



## The ASK-16 Motorized Glider: An Airborne Eddy Covariance Platform to measure Turbulence, Energy and Matter Fluxes

Inge Wiekenkamp<sup>1</sup>, Anna Katharina Lehmann<sup>2</sup>, Alexander Bütow<sup>6</sup>, Jörg Hartmann<sup>3</sup>, Stefan Metzger<sup>4,5</sup>,

5 Thomas Ruhtz<sup>2</sup>, Christian Wille<sup>1</sup>, Mathias Zöllner<sup>1</sup>, Torsten Sachs<sup>1</sup>

<sup>1</sup>GFZ German Research Centre for Geosciences, Telegrafenberg, 14473 Potsdam, Germany

<sup>2</sup>Department of Earth Sciences, Freie Universität Berlin, Berlin, Germany,

<sup>3</sup>Alfred Wegener Institute Helmholtz Centre for Polar and Marine Research (AWI), Am Handelshafen 12, 27570 Bremerhaven, Germany

10 <sup>4</sup>AtmoFacts, 3570 Larkspur Court, Longmont, CO 80503, USA

<sup>5</sup>Department of Atmospheric and Oceanic Sciences, University of Wisconsin-Madison, 1225 W Dayton St, 53711 Madison, WI, USA

<sup>6</sup>Atmospheric Physics Branch, Bundeswehr Geoinformation Centre, Frauenberger Straße 250, 53879 Euskirchen

Correspondence to: Inge Wiekenkamp ([inge.wiekenkamp@gfz-potsdam.de](mailto:inge.wiekenkamp@gfz-potsdam.de)) and Torsten Sachs ([15 \[potsdam.de\]\(mailto:potsdam.de\)\)](mailto:torsten.sachs@gfz-</a></p></div><div data-bbox=)

### Review Link for code and data:

Code: <https://dataservices.gfz->

[potsdam.de/panmetaworks/review/d90fd7b42934c80433fd023573467869deff28106003933100d7f2d78892c1fd/](https://dataservices.gfz-potsdam.de/panmetaworks/review/d90fd7b42934c80433fd023573467869deff28106003933100d7f2d78892c1fd/)

20 Data: <https://dataservices.gfz->

[potsdam.de/panmetaworks/review/d612e47508782aaca25613f742aadeecca78b0c93430e70912927aefa60a5140/](https://dataservices.gfz-potsdam.de/panmetaworks/review/d612e47508782aaca25613f742aadeecca78b0c93430e70912927aefa60a5140/)

**Abstract.** Airborne eddy covariance measurements can bridge the gap between local (tower-based) to regional (satellite/inversion-derived) flux data, as they provide information about the spatial distribution of turbulent fluxes for larger regions. Here, we introduce an airborne eddy covariance measurement platform based on an ASK 16 touring motor glider (TMG; also referred to as a power glider, hereafter referred to as motorized glider), which is equipped to measure the three dimensional wind vector, atmospheric conditions and derive airborne turbulent fluxes for the use of measurement campaigns over European landscapes. This study describes the measurement setup of the platform, and explains the workflows that were used to calculate and calibrate the three-dimensional wind vector, turbulent fluxes and their associated source areas. The glider is equipped with an 858 AJ Rosemount five-hole probe, a Picarro G2311-f gas analyser, a Novatel FlexPak G2-V2 GNSS-INS system, Vaisala temperature and humidity sensors (HMT311), and an OMEGA CHAL-003 thermocouple temperature sensor. Measurement data is processed with PyWingpod (python) and eddy4R (R) software packages to calculate wind vectors, turbulent fluxes, and assign footprints to the calculated fluxes. To evaluate the quality of the obtained fluxes, different quality assessments have been performed, including the determination of detection limits, spectral

25  
30  
35



analysis, stationarity tests, the analysis of integral turbulence characteristics, and measurement noise and error evaluation. The uncertainty of  $w$  is between 0.15 to 0.27 m/s (median = 0.23 m/s) and the uncertainty of  $u$  and  $v$  ranges between 0.16 to 0.55 m/s (median = 0.25 m/s). Analysis of exemplary flux data from flight transects indicates that the platform is capable of producing spatially highly resolved turbulent  
40 fluxes over heterogeneous landscapes. Overall, results from our analysis suggest that the ASK-16 airborne platform can measuring turbulent fluxes with a similar quality as earlier established high quality platforms.

## 1 Introduction

Eddy covariance is the standard method to quantify the exchange of energy and matter fluxes in the atmospheric boundary layer (Baldocchi, 2003; Rebmann et al., 2018) and to understand their environmental  
45 drivers (e.g. Jung et al., 2020; Xu et al., 2017). Deployed from flux towers, eddy covariance provides observations with a high temporal resolution, but the spatial coverage of these observations is limited (Kaharabata et al., 1997). Airborne eddy covariance measurements, on the other hand, can quantify fluxes from local to regional scale (e.g. Hannun et al., 2020; Metzger et al., 2013; Serafimovich et al., 2018; Zulueta et al., 2011), and can additionally capture dispersive fluxes (Metzger et al., 2021; Wolfe et al.,  
50 2018). Therefore, airborne eddy covariance measurements provide a perfect base to complement tower measurements and can be combined with tower data to gain information content (Metzger et al., 2021; Zulueta et al., 2011). In addition, airborne measurement systems provide high spatial flexibility and provide the opportunity to measure turbulent fluxes in landscapes that are normally difficult to access (e.g.  
55 Tetzlaff et al., 2015).

To date, a large variety of airborne eddy covariance platforms have been developed. The first platforms already measured turbulent fluxes more than 40 years ago (Desjardins et al., 1982; Lenschow et al., 1980). Over time, airborne flux measurement systems have evolved with the development of (1) modern measurement equipment (e.g. O'shea et al., 2013a; Wolfe et al., 2018), (2) flux quality assessment methods  
60 (Vellinga et al., 2013; Vickers and Mahrt, 1997; Mann and Lenschow, 1994), (3) flight pattern optimization (Metzger et al., 2021; Vihma and Kottmeier, 2000) and (4) the inclusion of wavelets in the flux calculation to obtain spatially highly resolved fluxes (Mauder et al., 2007; Metzger et al., 2017). Nowadays, modern airborne flux platforms can provide eddy covariance fluxes that are similar to high quality  
65 data from flux towers (e.g. Gioli et al., 2004). Operating platforms for airborne eddy covariance measurements include helicopter-borne turbulence probes (Helipod; Bange et al., 2006), weight-shift micro-light aircraft (Metzger et al., 2012; Metzger, 2013), drones (Sun et al., 2021), and different research aircraft (e.g. the NRC Twin Otter - Desjardins et al., 2016; Sky Arrow ERA - Gioli et al., 2006; Polar 5 - Hartmann et al., 2018; FAAM BAe-146 - O'shea et al., 2013b; NASA C-23 Sherpa - Wolfe et al., 2018).



70

Commonly, airborne eddy covariance campaigns focus on measuring sensible heat fluxes, latent heat fluxes and carbon fluxes in landscapes ranging from being relatively homogeneous to highly complex (e.g. Bange et al., 2006; Kirby et al., 2008; Metzger et al., 2013; Wolfe et al., 2018; Zulueta et al., 2013; Kohnert et al., 2017). A few airborne platforms have additionally been equipped with methane gas ana-  
75 lyzers to obtain methane fluxes for various landscapes, including arctic permafrost regions in Canada (Mackenzie Delta; Kohnert et al., 2017; Kohnert et al., 2018) and Alaska (Serafimovich et al., 2018; Zona et al., 2016; Sayres et al., 2017; Chang et al., 2014), wetlands (O'shea et al., 2013b; Hannun et al., 2020), gas extraction sites (Yuan et al., 2015), and agricultural landscapes (Desjardins et al., 2018; Hannun et al., 2020; Wolfe et al., 2018). Additional airborne eddy covariance campaigns have been performed to  
80 determine the regional fluxes of nitrogen oxides (NO<sub>x</sub>) in London (Vaughan et al., 2016; Vaughan et al., 2021), regional fluxes of volatile organic compounds (VOC) in Mexico City (Karl et al., 2009) and London (Vaughan et al., 2017) and regional ozone fluxes near Boulder (Lenschow et al., 1980). Overall, these examples show that airborne eddy covariance platforms are successful at providing regional turbulent fluxes of various compounds in a large variety of landscapes.

85

In this study, we equipped a Schleicher ASK-16 touring motor glider (operated by the Freie Universität Berlin, Germany) with sensors to measure turbulent fluxes of carbon, methane and energy at the regional scale. This new measurement platform enables a variety of research opportunities, including:

- (1) studying the comparability of tower fluxes and airborne fluxes and the spatial representativeness of  
90 eddy covariance towers;
- (2) studying the regional spatial distributions of energy and matter fluxes and their dominating (spatial) drivers;
- (3) applying and developing upscaling approaches to create regional scale surface flux maps;
- (4) comparing measured regional airborne fluxes with national inventory emission levels.

95 Additionally, several location-specific measurement flights were recorded between 2017 and 2022 to (1) study carbon and methane fluxes over differently managed peatland areas in northern Germany (2) evaluate the exchange of greenhouse gases between lake surfaces and the atmosphere (Germany).

This paper will introduce the new ASK-16 airborne measurement platform and the system specifications, including measurement equipment, precision and accuracy. Detailed descriptions of the (1) wind calibra-  
100 tion (2) wind calculation, (3) flux calculation and (4) footprint calculations are provided and the quality assessment of the different data products is described. To demonstrate the capability and the performance of this new airborne eddy covariance platform, different calibration and measurement flights are described and applied. Finally, to assess the quality, uncertainty and limitations of the measurement platform, the precision of the obtained wind vectors and fluxes is evaluated.

105



## 2 Methodology

### 2.1 The Aircraft and Measurement Setup

A Schleicher ASK-16 motorized glider (also known as powered glider; registration D-KMET; Alexander Schleicher GmbH, Poppenhausen, Germany) was deployed with a large set of sensors (Table 1) to measure airborne eddy covariance fluxes (Fig. 1). This motorized glider was manufactured in 1973, has a wingspan of 16 m, an airspeed ranging from 17.8 to 56 m/s (64 – 200 km/h) and is typically used for measurement operations of approximately 2 – 3 hours and can, depending on the weight and balance, fly up to 6 hours. The ASK-16 is operated by the Institute of Space Science at the Freie Universität Berlin, Germany and has mainly been used for in situ gas concentration and meteorological measurements in the past (e.g. measurements of cooling tower plumes as documented by Fortak (1975, 1976) or recently as part of the S-5p Campaign activities funded by the ESA, see <https://s5pcampaigns.aeronomie.be/>). In 2015, the aircraft had an extensive overhaul as a preparation for the currently presented measurement campaigns and other scientific missions.

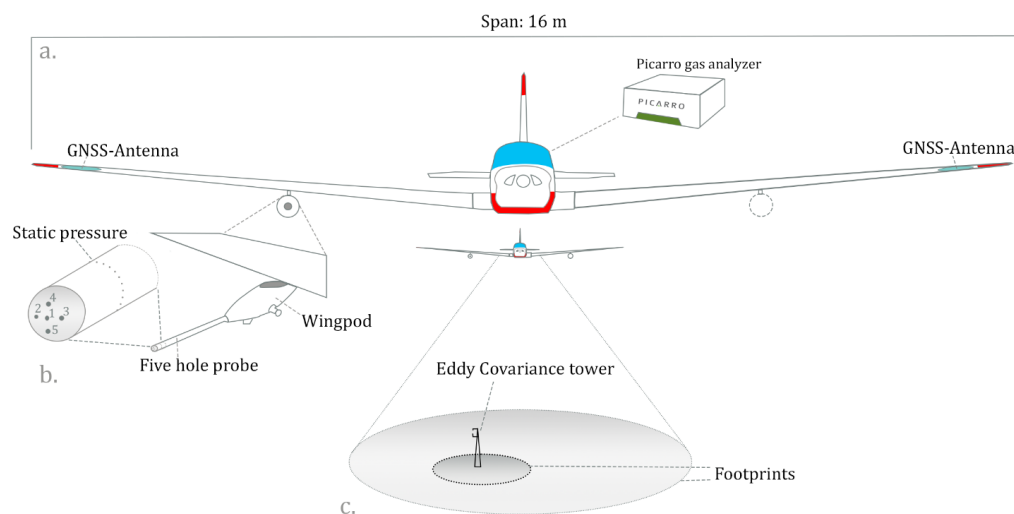


**Figure 1: Setup of the ASK-16 eddy covariance measurement platform** showing (a.) the general measurement setup (b.) the five-hole probe and (c.) a schematic representation of the footprint of such an airborne measurement platform in comparison to an eddy covariance tower. Keep in mind that the real difference in footprint magnitude depends on the measurement heights of the tower and the aircraft. More details about the instrumentation onboard the ASK-16 is provided in Table 1.



120

For airborne eddy covariance campaigns, the motorized glider is equipped with sensors to obtain high frequency fluctuations in wind, CO<sub>2</sub>, CH<sub>4</sub>, temperature and water vapor (Table 1 & Fig. 1). A Picarro G2311-f gas analyzer (Picarro Inc., Santa Clara, USA) is installed in the cabin of the ASK-16 to measure high frequency gas concentrations (10 Hz). On the front of the wingpod, an 858 AJ Rosemount five-hole probe (858 AJ, Rosemount Inc., Shakopee, USA) is mounted, which is connected to four CPT6100 pressure transducers (Mensor Corp., San Marcos, USA) located within the pod. Behind the pressure transducers, a SPAN-IGM-S1 system (Novatel, Calgary, Canada) is installed that integrates a combined GNSS + INS solution. Global Navigation Satellite Systems (GNSS) antennas are installed in the wings of the motorized glider, which are connected with the IMU and the satellite receiver. To increase the GNSS position and angle accuracy, a second GPS receiver was connected to the GNSS-INS system (FlexPak G2-V2; Novatel, Calgary, Canada). Additionally, the wingpod contains a Pt100 RTD temperature sensor (Class F0.1 IEC 60751, Vaisala, Helsinki, Finland) and HUMICAP humidity sensor (Vaisala, Helsinki, Finland), which are connected to a HMT311 temperature and humidity transmitter (Vaisala, Helsinki, Finland). In 2019, a CHAL-003 thermocouple temperature sensor (OMEGA, Deckenpfronn, Germany) was additionally installed on the outside of the wingpod, close to the file-hole-probe to measure high frequency temperature and calculate sensible heat fluxes. All time stamps of the sensor blocks are synchronized to the inertial navigation system.

Table 1: Overview of installed sensors on the ASK-16 eddy covariance measurement platform, including model and the manufacturer information. Additional information about the measured variables and their accuracy and precision is given in Table 2.

Component	Model	Manufacturer
Gas analyzer	Picarro G2311-f	Picarro Inc., Santa Clara, USA
Board computer	Raspberry Pi 3 Model B	Raspberry Foundation, Cambridge, Great Britain
Five hole probe	858 AJ Rosemount	Rosemount Inc., Shakopee, USA
Pressure sensor	Mensor CPT6100	Mensor Corp., San Marcos, USA
USB converter (pressure)	USB COM232PLUS4	FTDI, Glasgow, Great Britain
SPAN GNSS+INS system	SPAN-IGM-S1 with FlexPak-G2-V2 & IMU-IGM-A1	Novatel, Calgary, Canada
Thermocouple	CHAL-003	OMEGA, Deckenpfronn, Germany
Temperature setpoint conditioner	AD596/AD597	Analog Devices, Wilmington MA, USA
USB-adapter thermocouple	Redlab USB-1608FS-PLUS	Meilhaus Electronic GmbH, Alling, Germany
TAT sensor housing	Rosemount 102E	Rosemount Inc., Shakopee, USA
Humidity sensor	HUMICAP	Vaisala, Helsinki, Finland
Temperature sensor	Pt100 RTD Class F0.1, IEC 60751	Vaisala, Helsinki, Finland
Humidity transmitter	HMT311	Vaisala, Helsinki, Finland

140



*Table 2: Overview of the recorded variables, recording frequency, measurement range and the accuracy and the precision of the measurement. In most cases, measurement uncertainty and range was obtained from datasheets from the manufacturers (PICARRO, Vaisala, Novatel, Mensor, Omega, Rosemount), and from Buetow (2018), Lehmann (2022), National Institute for Standards and Technology (1999) and Yang et al. (2016). The precision of recorded variables from the INS-GNSS (indicated with \*\*) were obtained from on-ground measurements on the 04.05.2022 in Lüsse, Germany, where the aircraft remained stationary for ca. 1 hour.*

Recorded Variable	Sensor	Unit	Recording Rate	Measurement Range	Accuracy (Bias)	Precision
Atm. CO <sub>2</sub> concentration	Picarro G2311-f	ppm (dry mole fraction)	10 Hz	300–500 ppm	-	0.2 ppm ( $\tau$ : 0.15 ppm, noise: 0.0023 ppm <sup>2</sup> /Hz)
Atm. CH <sub>4</sub> concentration	Picarro G2311-f	ppm (dry mole fraction)	10 Hz	100 - 300 ppb	-	3 ppb ( $\tau$ : 1.1 ppb, noise: 0.23 ppm <sup>2</sup> /Hz)
Atm. H <sub>2</sub> O concentration	Picarro G2311-f	% (of volume)	10 Hz	0 - 99 % RH	-	0.30%
Static pressure	CPT6100	Pa	50 Hz	552 - 1172 hPa	0.01%	0.004%
Differential pressure alpha	CPT6100	Pa	50 Hz	-35 - 35 hPa	0.01%	0.004%, 0.26 Pa **
Differential pressure beta	CPT6100	Pa	50 Hz	-35 - 35 hPa	0.01%	0.004%, 0.73 Pa **
Dynamic pressure	CPT6100	Pa	50 Hz	0 - 70 hPa	0.01%	0.004%, 0.39 Pa **
Relative humidity	HMT310 - HUMICAP	%	20 Hz	0 - 100% RH	0.6 - 1.0 %	0.5 – 0.85 %
Temperature (slow)	HMT310 - Pt100	°C	20 Hz	- 40 - 60 °C	0.2°C	0.2 °C- 0.5 °C
Temperature (fast)	CHAL-003	°C	50 Hz	- 20 - 60 °C	1.1°C or 0.4%	1°C
Latitude	SPAN GNSS+INS	deg [WGS 84]	20 Hz	± 89.9 °	0.000017 ° (1.2 m)	0.0000017 ° **
Longitude	SPAN GNSS+INS	deg [WGS 84]	20 Hz	± 180 °	0.000017 ° (1.2 m)	0.0000054 ° **
Height	SPAN GNSS+INS	m.a.s.l.	20 Hz	0 - 80000	0.6 m	0.39 m **
Northward aircraft velocity	SPAN GNSS+INS	m/s	20 Hz	0 - 515 m/s	0.02 m/s	0.0038 m/s **
Eastward aircraft velocity	SPAN GNSS+INS	m/s	20 Hz	0 - 515 m/s	0.02 m/s	0.003 m/s **
Vertical aircraft velocity	SPAN GNSS+INS	m/s	20 Hz	0 - 515 m/s	0.01 m/s	0.0035 m/s **
True heading	SPAN GNSS+INS	rad	20 Hz	0 – 360 °/0 - 2 $\pi$	0.015 rad	0.0001 rad **
Pitch angle	SPAN GNSS+INS	rad	20 Hz	± 90 °	0.035 rad	0.007 rad **
Roll angle	SPAN GNSS+INS	rad	20 Hz	± 180 °	0.035 rad	0.00017 rad **



All sensors in the wingpod are connected to a Raspberry Pi 3 (Model B; Raspberry Pi Foundation, Cambridge, United Kingdom) through Universal Serial Bus (USB) interfaces (see Table 1). Data logging is managed with *hgpstools* (<https://bitbucket.org/haukex/hgpstools>, developed by Hauke Dämpfling, Leibniz Institute of Freshwater Ecology and Inland Fisheries (IGB), Berlin, Germany), an open source software package written in Perl. The software manages the communication between the single board computer (Raspberry Pi) and the sensors. Table 2 provides a full list of all recorded variables, their measurement frequency and measurement uncertainty.

## 2.2 Data Processing: eddy4R and PyWingpod

To process the data and calculate wind vectors and turbulent fluxes, two software packages were used in this study: *eddy4R* (Metzger et al., 2017) and *PyWingpod*. Figure 2 shows the entire data processing procedure for the ASK-16 flight data: from raw data to wind vector data to calculated flux output. It shows which processing steps are performed by which software package and what output data is generated. The structure of this paper follows the processing steps visualized in Fig. 2.

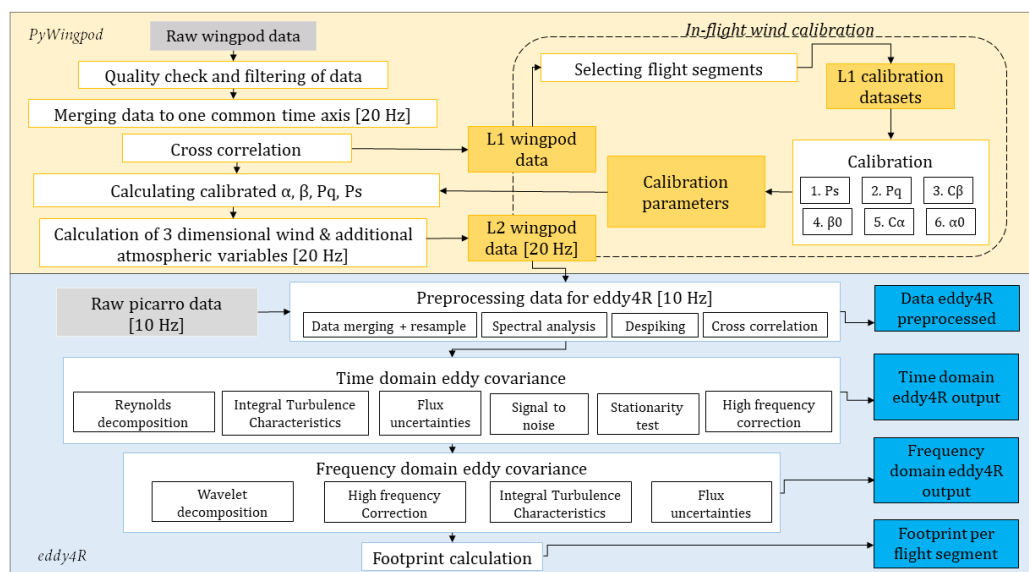


Figure 2: Workflow ASK-16 platform for processing airborne eddy covariance data. The yellow section describes workflows performed in the Python toolbox *PyWingpod*. The blue region shows the workflow as performed in *eddy4R* (Metzger et al., 2017). Coloured boxes display input/output of by the software: grey boxes represent raw input; yellow boxes represent output created by *PyWingpod*, whereas blue boxes present output created by *eddy4R* packages.



First, the data was processed with the *PyWingpod* toolbox, developed in Python (version > 3.7) by the German Research Centre for Geosciences (GeoForschungsZentrum Potsdam) and the Free University of Berlin (Freie Universität Berlin) to specifically process the wingpod data of the ASK-16. This software package includes different libraries created for the preprocessing and calibration of the wingpod data. It also incorporates functions to calculate the final wind vector and additional meteorological variables, which are partially based on functions in EGADS, version 0.8.9 (EUFAR General Airborne Data-processing Software), a Python based toolbox for processing airborne atmospheric data which can be accessed via GitHub (<https://github.com/EUFAR/egads>). The software package *PyWingpod* provides several additional functions to visualize the data during these different data processing steps, and can generate additional output (e.g. figures, tables, .kml files and shapefiles), which can be used for further data exploration.

Afterwards the wind vector output and wingpod data was merged with Picarro data and further processed in *eddy4R* (Metzger et al., 2017) to calculate fluxes and footprints. *eddy4R* consists of a family of EC code packages (currently: *eddy4R.base*, *eddy4R.qaqc*, *eddy4R.stor*, *eddy4R.erf*, *eddy4R.turb* and *eddy4R.ucrt*), each consisting of a set of functions that have been developed in the open-source R language (R Core Team, 2021). Using a combination of functions from the *eddy4R* universe, wavelet-based fluxes, Reynolds fluxes, and footprints were calculated, and a quality and uncertainty assessment of the fluxes was performed (Fig. 2 – blue region).

### 2.3 Wind Vector Calculation

One of the two main components of the eddy covariance technique is the measurement of the turbulent wind vector at high frequency (Vellinga et al., 2013), for which we used the calculations as described in detail by Lenschow (1986) and Lenschow and Spyers-Duran (1989). As the wind vector is measured from a moving platform (motorized glider), the wind vector ( $V_{wind}$ ) is calculated as a difference between the true airspeed ( $V_{tas}$ ; measured by the five-hole probe) and the groundspeed ( $V_{gs}$ ; measured by the GNSS & INS system) according to the following equation:

$$V_{wind} = V_{gs} - V_{tas} + \Omega * L \quad (1)$$

185

The displacement-term  $\Omega * L$  accounts for the displacement between the INS- GNSS and the five-hole probe, where  $L$  describes the lever arm length (distance between accelerometer and five-hole probe, here 0.85 m) and  $\Omega$  represents the angular velocities of the motorized glider (Mallaun et al., 2015). A more





detailed description of the wind calculation procedure can be found in Lenschow and Spyers-Duran  
190 (1989).

## 2.4 Measurement Calibration

To eliminate aerodynamic **position** errors of the five-hole probe, several calibration flights were per-  
formed in order to increase the accuracy of the calculated 3-dimensional wind vector. Calibration was  
performed on the static pressure ( $p_s$ ), dynamic pressure ( $p_q$ ), and the differential pressure measurements  
195 ( $p_\alpha$  - alpha pressure, and  $p_\beta$  - beta pressure) to improve  $V_{tas}$ . As you can see in the calibration equations  
below,  $p_\alpha$  and  $p_q$  are used for the calculation of the angle of attack ( $\alpha$ , see equation 2) and  $p_\beta$  and  $p_q$  are  
used for the calculation of the sideslip angle ( $\beta$ , see equation 3):

$$\alpha = \frac{p_\alpha}{C_\alpha p_q} - \alpha_0 \quad (2)$$

200

Here,  $C_\alpha$  and  $\alpha_0$  are the calibration parameters, which describe the sensitivity to the inverse slope of  $p_\alpha$   
and the offset of the angle of attack.

$$\beta = \frac{p_\beta}{C_\beta p_q} - \beta_0 \quad (3)$$

205

In this equation,  $C_\beta$  describes the inverse slope of  $p_\beta$  in the calibration equation and  $\beta_0$  the offset.

The calibration of the pressure measurements is an important procedure for airborne eddy covariance  
measurements, as the calculated wind is highly sensitive to input uncertainties (see e.g. Metzger et al.,  
210 2011). In this paper, we focus on describing the on-ground and in-flight calibration procedures applied  
for ASK-16 wingpod data specifically. Detailed descriptions of all available state-of-the-art in-flight cal-  
ibration procedures are for example provided by Drüe and Heinemann (2013), Vellinga et al. (2013), and  
Mallaun et al. (2015).

### 2.4.1 Time Alignment Wingpod Data

215 Time lags between sensors can be caused by differences in processing speeds of different sensors (Drüe  
and Heinemann, 2013). Although these lags are mostly small (< 1 second; Drüe and Heinemann, 2013),  
such lags need to be detected, as time alignment is crucial to ensure an accurate wind and reliable turbulent  
fluxes. Therefore, potential time lags between measurement data recorded by different devices were as-  
sessed before other calibration procedures were performed. To assess the time alignment of the sensors,  
220 the assumption was made that measurements from the same measurement group (A/D converter or sensor  
block) should have the same lag, which is similar to the approach used by Drüe and Heinemann (2013).



In our case, we assessed the time lags for four different sensor groups: pressure sensors (block 1), INS-  
225 SS sensors (block 2), temperature sensors (block 3) and all HMT Vaisala sensors (block 4). While performing cross-correlation analysis for the different sensor groups, no clear lags were observed between any of the wingpod's sensor groups. Therefore, no time shifts were applied to any of the four sensor groups within the wingpod.

#### 2.4.2 On-Ground Calibration Wingpod Data

Before in-flight calibration maneuvers were analyzed, on-ground calibration was performed to correct for potential offsets in the pressure sensor data. Such offsets can affect the final wind vector and therefore  
230 need to be determined. Before the start of a measurement flight, the wind inflow into the pressure holes was covered by placing a glass fiber composite non-airtight cap onto the five-hole probe. The on-ground pressure data for this wind-free period was afterwards analyzed to characterize the bias in dynamic pressure ( $q_i$ ),  $\alpha$  pressure ( $p_\alpha$ ) and  $\beta$  pressure ( $p_\beta$ ). In this setup, the static pressure offset could not be assessed. For the available datasets, we mostly used a 30 minute pressure record to determine the offsets. If  
235 the duration of the on-ground and wind-free period was shorter, we used the available time-frame with stable measurements, with the restriction of having at least 10 minutes of data. In our case, the pressure offsets were very small and ranged between 1 to 10 Pa for the different pressure measurements.

#### 2.4.3 In-Flight Calibration Maneuvers

In our study we used five in-flight calibration maneuvers (reverse heading, pitching, yawing, and speed  
240 maneuvers, and wind squares) for the calibration of pressure measurements ( $q_i$ ,  $q_s$ ,  $q_\alpha$  and  $q_\beta$ ), the corresponding  $\alpha$  and  $\beta$  angles (see section 2.4), and for the evaluation of the calibration procedure (Fig. 3). Each individual in-flight calibration procedure mainly focuses on the calibration of a single variable, while trying to rule out or minimize the effect of external factors on that specific calibration parameter.

245 During a speed maneuver (Fig. 3a), the speed of the aircraft is first slowly increased (acceleration segment), and afterwards slowly decreased (deceleration segment) at a relatively constant altitude. This procedure is repeated multiple times to study the effect of speed variations on the different pressure measurements of the five-hole probe ( $\alpha$ ,  $P_q$  and  $P_s$ ). During a pitching maneuver (Fig. 3b), the nose of the aircraft moves sinusoidal upwards and downwards by the deflection of the aircraft's elevator. The airplane  
250 is turning around its lateral axis, altering the pitch angle ( $\theta$ ) of the aircraft, and induces a change in the angle of attack ( $\alpha$ ). This maneuver is used for the calibration of  $\alpha$ , and uses the concept that pitch oscillations should not significantly affect the vertical wind measurement ( $w$ ).

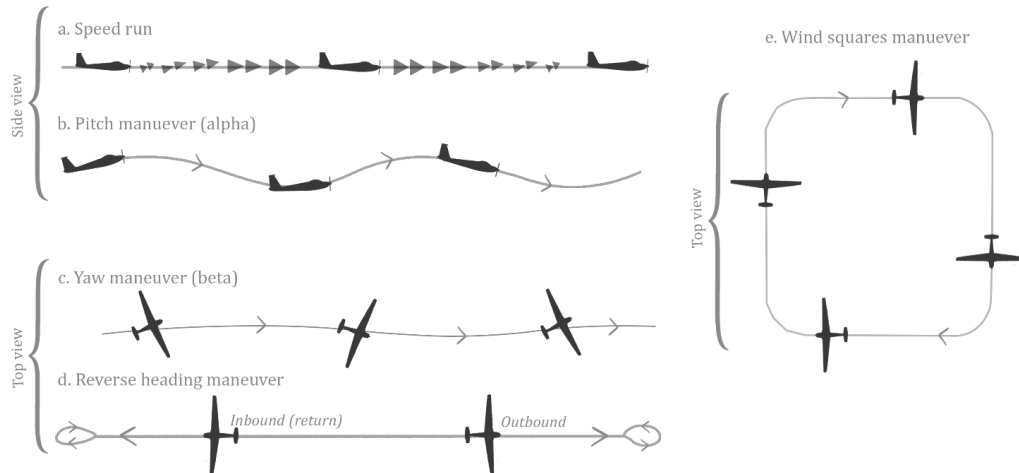


**Figure 3:** Schematic illustration of flight maneuvers performed with the ASK-16 to calibrate the pressure measurements of the five-hole probe, including speed runs (a.), yaw and pitch maneuvers (b. and c.), reverse heading maneuvers (d.) and wind squares (e.).

255

Yawing maneuvers (Fig. 3c), on the other hand, are performed to calibrate the sideslip angle ( $\beta$ ). During a yawing maneuver, the aircraft is rotated harmonically sinusoidal around its vertical axis (heading; nose moving left/ right) by engaging the rudder and aileron(s). The aircraft is kept at a (more or less) constant altitude. To calibrate for  $\beta$ , we use the assumption that the horizontal components of the wind ( $u, v$ )

260

should not be affected by yaw maneuvers. Reverse heading maneuvers (Fig. 3d), also called return track flights (Hartmann et al., 2018), were performed for the calibration of the dynamic pressure ( $q_i$ ),  $\beta$  and  $\alpha$  angles. The aim of this maneuver is to fly two times through a very similar air mass, while keeping the time difference between the outbound and return flight as small as possible. Wind squares (Fig. 3e) are box shaped flight patterns, where the airplane flies four times a straight track, separated by  $90^\circ$  turns.

265

During this maneuver, altitude and airspeed are kept as constant as possible. In our case, the maneuver was used as a second check to assess the quality of the calibration procedure (see section 2.6).

As several of the in-flight calibrations require the calculation of an a-priori wind, the order of the calibration procedure can slightly affect the calibration outcome. Here, the order of the calibration was based in first instance on a sensitivity analysis (Lehmann, 2022) starting with the two least sensitive parameters (here: static pressure and dynamic pressure). Due to the difference in magnitude and importance of the wind components for airborne eddy covariance flux calculations, we furthermore first optimized the parameters related to the horizontal wind components ( $C_\beta$  and  $\beta_0$ ) and then optimized the parameters that

270



are directly connected to vertical wind component ( $C_\alpha$  and  $\alpha_0$ ), as proposed by Metzger et al. (2011).

275 Although cross-dependences in the calibration procedure can be dealt with by iteratively optimizing the calibration (Metzger et al., 2011), this was not performed in our study. Here, we assume that the range and amount of calibration maneuvers will be sufficient to obtain suitable calibration parameters during different flight conditions.

280 Flight maneuver data were processed with the *PyWingpod* Python software package (Wiekenkamp et al., 2024a) to determine the calibration coefficients as described in the upcoming sections. In this study, no wind tunnel experiments were performed, but results from earlier studies (both wind tunnel experiments and in-flight calibrations) were used as a reference. As the wingpod of the ASK-16 was first installed in 2017 and re-installed in 2019, two calibration parameter sets were calculated for the static pressure, dynamic pressure,  $\alpha$ , and  $\beta$  (calibration parameters for 2017-2018 and calibration parameters for 2019-2022).

#### 2.4.4 Static Pressure Calibration

Although the static pressure measurement should represent that of a free airstream, the measured static pressure can be influenced by the flow around the aircraft, causing it to differ from the ambient static pressure. This pressure deviation is often referred to as static pressure defect ( $p_{s,err}$ ) and needs to be defined to adjust the measured static pressure. Past research has shown that the static pressure defect depends on (1) the speed of the aircraft, but also on (2) changes in the flow angles  $\alpha$  and  $\beta$  (Bögel and Baumann, 1991; Drüe and Heinemann, 2013; Tjernström and Friehe, 1991). In this study, the static pressure defect ( $p_{s,err}$ ) is determined via speed runs (at relatively constant altitude) and yawing maneuvers, according to Kalogiros and Wang (2002). Speed maneuvers were used to assess the effect of the airplane on speed fluctuations (recorded in the dynamic pressure) and the effect of different  $\alpha$  flow angles on the static pressure. Yaw maneuvers were used to assess the effects of different  $\beta$  flow angles on the static pressure. Data from each single maneuver was used to fit the following polynomial equation:

$$300 \quad p_{s,err} = (a_1 * p_q) + (a_2 * p_q * p_\alpha^2) + (a_3 * p_q * p_\beta^2) \quad (4)$$

where  $p_q$  represents the dynamic pressure,  $a_{1-3}$  are the calibration parameters and  $p_\beta$  and  $p_\alpha$  are the differential pressure measurements. Speed maneuvers were used to determine  $a_1$  and  $a_2$ , yaw maneuvers were used to calibrate  $a_3$ . During the determination of calibration parameters for each single maneuver, 305 the calibration data were offset corrected (resulting in an absolute offset of 0). To exclude the influence of following calibrations ( $C_\alpha, C_\beta, \alpha_0$  and  $\beta_0$ ) on the adjusted pressure, possible influences of sideslip and angle of attack on the static pressure were accounted for using the differential



pressure measurements  $p_\alpha$  and  $p_\beta$ . To rule out the influence of altitude fluctuations during the speed maneuvers, the static pressure was first normalized by altitude. Here, the barometric pressure was calculated  
310 for the assigned measurement height. Afterwards, a polynomial function was fitted between the normalized static pressure (independent variable) and one or multiple dependent variables ( $p_\alpha$ ,  $p_\beta$  and  $p_q$ ), resulting in a function that can be used to correct the measured static and dynamic pressure.

#### 2.4.5 Dynamic Pressure Calibration

The dynamic pressure calibration was performed in two steps. First, the dynamic pressure was adjusted  
315 by adding the static pressure defect (section 2.4.4, Eq. 4) to the dynamic pressure measurement. Afterwards, we used the dynamic pressure calibration method as proposed by Hartmann et al. (2018), using the assumption that the average groundspeed over an outbound (vector index 1) and return flight (vector index 2) is equal to the average true airspeed:

$$320 \quad \frac{1}{2} * \left( \frac{v_{gs,1}}{\cos(\gamma)} + \frac{v_{gs,2}}{\cos(\gamma)} \right) = \frac{1}{2} * (|v_{tas,1} + v_{tas,2}|) = v_{ref} \quad (5)$$

Based on the magnitude of the drift, the difference between  $\chi$ , the true track and  $\theta$ , the true heading ( $\chi - \theta = \gamma$ ), we needed to include  $\cos(\gamma)$  in our equation (Eq.5). Afterwards, the reference undisturbed dynamic pressure ( $p_{q,ref}$ ) was determined using the following equation:

$$325 \quad p_{q,ref} = \frac{1}{2} * \frac{1}{\rho * v_{ref}^2} \quad (6)$$

Next, we plotted the average measured dynamic pressure ( $p_{q,i}$ ) against the reference undisturbed pressure ( $p_{q,ref}$ ) to calculate a correction factor ( $c_q$ ):

$$330 \quad p_{q,ref} = c_q * p_{q,i} \quad (7)$$

This calculated correction factor was then used to adjust the measured dynamic pressure.

#### 2.4.6 $C_\beta$ and $\beta_0$ Calibration

335 Similar to the static and dynamic pressure, angle of attack and sideslip angle are affected by pressure field deformations around the aircraft, which can cause deviations between the measured and the real  $\alpha$  and  $\beta$  angles (Drüe and Heinemann, 2013). To correct for these deviations, the sideslip angle was calibrated using equation 3. To determine  $C_\beta$ , yawing maneuvers were used, which are commonly applied for such calibration (e.g. Bögel and Baumann, 1991; Drüe and Heinemann, 2013; Mallaun et al., 2015; Williams



340 and Marcotte, 2000). In a first step, the wind vector is calculated for a yawing maneuver. Afterwards, the  
sum of the standard deviation in the horizontal wind components  $u$  and  $v$  is calculated. Iteratively, this  
summed standard deviation is optimized using the Nelder-Mead optimization algorithm in SciPy  
(Virtanen et al., 2020).

345 To determine  $\beta_0$  (the offset of  $\beta$ ), we used a set of outbound and return flights (reverse heading maneu-  
vers). Here, the difference between the average horizontal wind components ( $u$  and  $v$ ) was iteratively  
minimized for each maneuver (Williams and Marcotte, 2000; Drüe and Heinemann, 2013) using the  
Nelder-Mead optimization method in SciPy (Virtanen et al., 2020). As local flight conditions and the  
selection of the exact flight segments can affect the outcome of the  $\beta_0$  optimization, the mean  $\beta_0$  was  
350 calculated from a large set of reverse heading maneuvers.

#### 2.4.7 $C_\alpha$ and $\alpha_0$ Calibration

The calibration of the angle of attack  $\alpha$  was performed using a variety of calibration methods. Similar to  
the correction of the sideslip angle, the angle of attack can be calibrated, using equation 2. First  $C_\alpha$  is  
determined using flight data from slow pitching maneuvers. For these flight maneuvers, first the vertical  
355 wind speed was calculated, using an offset of 0 ( $\alpha_0$ ) and the manufacturer-supplied correction factor of  
0.079 [1/°] as provided by Rosemount (Drüe and Heinemann, 2013). Here, we assumed that the obtained  
variability in vertical wind speed was mainly caused by the movement of the airplane and should be  
minimized (Bögel and Baumann, 1991; Mallaun et al., 2015). Therefore, we optimize the sensitivity pa-  
rameter  $C_\alpha$  iteratively by minimizing the standard deviation of the vertical wind ( $w$ ) with the Nelder-  
360 Mead optimization algorithm in SciPy (Virtanen et al., 2020).

Afterwards, we used flight data from straight level flights with small speed variations to obtain a calibra-  
tion parameter for  $\alpha_0$ . This second calibration procedure assumes that if we fly long enough over a straight  
track, the average vertical wind component should ideally reach 0. Therefore, we first calculate the aver-  
365 age windspeed over the flight segment without offset, and then iteratively optimize  $\alpha_0$  by minimizing the  
absolute average vertical wind component.

As an alternative approach, data from speed maneuvers and/or reverse heading maneuvers can be used to  
calibrate  $\alpha$ , as proposed by Hartmann et al. (2018). For this calibration procedure, we used the fact that,  
370 without aircraft pressure field deformations, the angle of attack equals the pitch angle ( $\frac{p_\alpha}{p_q} = \theta$ ). This is  
only valid during straight level flights, and for fixed-wing aircrafts, where  $\alpha$  varies with airspeed. Similar  
to Hartmann et al. (2018), speed maneuver data was first used to assign the relationship between  $\frac{p_\alpha}{p_q}$  and  
 $\theta$ , while accounting for vertical movement of the plane ( $w_p$ ). Based on the obtained relationship,  $C_\alpha$  and



$\alpha_0$  were calculated. In a second step, we selected flight sections where the vertical movement of the plane  
375 was less than 1.5 m/s.

## 2.5 Flux and Footprint Calculation

After the wind data was calibrated and the three-dimensional wind vector was calculated, this data (10  
380 was merged with data from the Picarro gas analyzer (10 Hz). In this case, a nearest neighbor interpo-  
lation is applied to bring both datasets on a common time axis with a resolution of 10 Hz and retain the  
amplitude of the original measurements. Subsequently, outliers were detected in the different data prod-  
ucts using a nonlinear median filter algorithm with a window of 7 points ( $N = 3$ ) according to Brock  
(1986) and Starkenburg et al. (2016). Afterwards, two types of flight segments are extracted from the  
combined dataset: (1) vertical flight segments and (2) straight level segments (legs). Data from vertical  
flight segments (potential temperature, relative humidity,  $\text{CH}_4$  and  $\text{CO}_2$  concentrations) is used to infer  
385 the thickness of the atmospheric boundary layer. Straight, horizontal flight segments (legs) are further  
processed to calculate surface fluxes.

Data from flight legs were further used for flux processing with *eddy4R* (Metzger et al., 2017). Lag times  
were obtained for every flight leg by performing a high-pass filtered cross-correlation between  $w'$  and  
390 the gas concentrations ( $\text{H}_2\text{O}$ ,  $\text{CO}_2$  and  $\text{CH}_4$ ) as proposed in Hartmann et al. (2018).  $\text{CO}_2$  and  $\text{CH}_4$  concen-  
trations were afterwards shifted according to the median lag of a particular flight. As the latency of  $\text{H}_2\text{O}$   
can be variable within a single flight, no median lag for an entire flight was applied. Instead, individual  
lags were assigned for each individual flight leg of a specific flight. No lag correction was applied to the  
temperature data, as no clear lag could be determined between  $w'$  and  $T'$ .

395

The flux calculation for each leg was performed with the *eddy4R* (Metzger et al., 2017) packages accord-  
ing to Metzger et al. (2012) and Metzger et al. (2013), following the workflow as shown in Fig. 2. Alt-  
though Airborne fluxes are also calculated using a time domain-based approach, the focus here is on the  
fluxes calculated with a time-frequency domain (wavelet) based approach. This wavelet based approach  
400 is explained in detail by Metzger et al. (2013). In short, a continuous wavelet transform approximation  
according to Torrence and Compo (1998) was performed for all relevant variables ( $u$ ,  $w$ , Temperature,  
 $\text{H}_2\text{O}$ ,  $\text{CO}_2$  and  $\text{CH}_4$ ) using the Morlet wavelet as mother wavelet. Afterwards, a cross-scalogram was  
calculated using the measured vertical wind and a second scalar (here: Temperature,  $\text{H}_2\text{O}$ ,  $\text{CO}_2$  and  $\text{CH}_4$ ).  
Next, the integral of the cross-scalogram was calculated at the original resolution and for each flux seg-  
405 ment using a given window size. Based on the flight altitude of the ASK-16 (ca. 150-250 m. above the  
surface), fluxes were calculated every 200 meters with an overlapping moving window of 2000 meters.  
Using a time-frequency resolved version of the eddy covariance methods results in a higher spatial dis-  
cretization where multiple flux segments are calculated for a single leg. Using wavelets, contributions



410 from the longer wavelengths (large eddies) can be incorporated in these flux segments. Instead of obtain-  
only a single flux estimation per flight leg, we can now obtain an entire transect of fluxes.

Footprints were calculated by combining the Kljun et al. (2004) along-wind footprint with a Gaussian cross-wind distribution function as described in Metzger et al. (2012). This combination makes the footprint formulation more applicable for higher altitudes and thus for airborne eddy covariance. Inputs for  
415 the calculated footprint function include (1) the measured friction velocity, (2) measurement altitude, (3) the standard deviation of the lateral and vertical wind ( $\sigma v$ ,  $\sigma w$ ), (4) the boundary layer height, and (5) the calculated roughness length according to Högström (1988). After the calculation of the footprints, single segment footprints, leg-integrated footprints, and flux-footprints (flux\*footprint) were calculated. This will enable us to create follow-up products, such a flux-topographies (e.g. Kohnert et al., 2017) or inte-  
420 gration with earth observations to regional flux maps through physics-guided artificial intelligence (e.g. Metzger et al., 2013; Serafimovich et al., 2018; Vaughan et al., 2021).

## 2.6 Measurement Accuracy and Quality Assessment

To obtain information about the quality and uncertainty of the measurements during the flights, several analyses were performed for individual flights and single flight legs. Airborne turbulent fluxes that are  
425 obtained by using the eddy covariance method are only valid under (1) steady state conditions with (2) developed turbulence (Foken, 2017). To evaluate the flight conditions, the integral turbulence characteristics were calculated and stationarity was assessed. Stationarity was assessed using (1) a trend analysis and (2) an internal in-stationarity analysis according to Foken and Wichura (1996) and Vickers and Mahrt (1997). For each flight segment, Integral Turbulence Characteristics were calculated for measured and  
430 modelled  $u$ ,  $w$  and  $u^*$  according Thomas and Foken (2002). Leg segments that surpassed the threshold above 100% were flagged.

Besides flight conditions, measurement errors and flux detection limit are important, as they provide information about the potential and limitations of the measurement platform. Flux detection limits were  
435 calculated for each single flight leg by performing a random flux uncertainty estimation according to Billesbach (2011). Here, a random flux uncertainty estimation is used where fluxes are recalculated for randomly shifted time series to assess the flux detection limits. Systematic and random statistical errors were calculated according to Mann and Lenschow (1994) and Lenschow and Stankov (1986). Finally, spectral characteristics of the individual measured gasses and wind components was assessed by looking  
440 at the spectra of the wind components, fast temperature and measured gases, as performed e.g. by Hartmann et al. (2018), Metzger et al. (2011) and Wolfe et al. (2018).





### 3 Results and Discussion

#### 3.1. Wind Calibration Results

445 In this study, the calibration of the static and dynamic pressure, as well as sideslip angle and angle of  
 attack was performed following the calibration scheme in Fig. 2, as described in detail in the methodology  
 of this paper. For the calibration of all pressure sensor related calibration parameters, pitching maneuvers,  
 yawing maneuvers, reverse heading maneuvers and speed maneuvers were used (see section 2.4.3. –  
 2.4.7). Information about the meteorological conditions during these flight maneuvers is provided in the  
 450 supplement A: Flight Maneuver Information. Whereas metadata and calibration results from single cali-  
 brations are provided in Supplement A, median calibration values and standard deviations that were as-  
 signed to the calibration periods 2017/2018 and 2019/2022 are given in Table 3. The description and  
 discussion of the calibration results follows the order of calibration.

**Table 3:** Overview of obtained calibration parameters for the different monitoring periods (2017-2018 and 2019 – 2022) and their uncertainty (described by standard deviation  $\sigma$  of all obtained parameters obtained during the specific flight period). Final calibration parameters are described here by the median of all parameters that were obtained for the particular flight period (See supplement tables, Supplement A, indicated here by S. Table). Values in brackets ( $C\alpha$  and  $\alpha 0$ ) present the calibration parameters obtained from the speed runs (see Figure 8 and section 3.1.4).

455

	2017/2018	$\sigma$ 2017/2018	Data	2019 - 2022	$\sigma$ 2019-2022	Data	Cal. Eq.	S. Table
<b><math>C\alpha</math></b>	0.091 (0.1)	$\pm 0.033$	4 pitching maneuvers	0.091 (0.095)	$\pm 0.015$	3 pitching maneuvers	2	S5
<b><math>\alpha 0</math></b>	5.46 (5.6)	$\pm 0.11$	28 flight legs	5.66 (5.7)	$\pm 0.32$	46 flight legs	2	S3
<b><math>C\beta</math></b>	0.071	$\pm 0.0008$	5 yawing maneuvers	0.071	$\pm 0.001$	4 yawing maneuvers	3	S2
<b><math>\beta 0</math></b>	-0.75	$\pm 0.29$	14 reverse heading maneuvers	-0.76	$\pm 0.9$	23 reverse heading maneuvers	3	S3
<b><math>Cq</math></b>	0.99	$\pm 0.0002^*$	14 reverse heading maneuvers	0.99	$\pm 0.0004^*$	23 reverse heading maneuvers	5-7	S3, S4
<b><math>a1</math></b>	0.046	$\pm 0.002$	2 speed maneuvers	0.0465	$\pm 0.007$	10 speed maneuvers	4	S1
<b><math>a2</math></b>	-2.01	$\pm 0.04$	2 speed maneuvers	-2.11	$\pm 0.28$	10 speed maneuvers	4	S1
<b><math>a3</math></b>	-1.25	$\pm 0.16$	5 yawing maneuvers	-1.58	$\pm 0.09$	4 yawing maneuvers	4	S2



### 3.1.1 Static Pressure

460 The blue dots in the figure present the measured data and the black dots represent the fitted relationship  
 (polynomial function).

The static pressure defect was assessed using data from twelve speed runs and nine yawing maneuvers that were performed over northern Germany between 2017 and 2022 (for more details, see Supplement A, Table S1 and Table S2), of which most speed runs were performed in 2019. Overall, external factors  
 465 that could affect the calibration were relatively small, and likely did not have a large effect on the determination of the static pressure defect. In most cases, speed runs were performed at an altitude of approximately 1000 - 1100 m.a.s.l., the maximum change in groundspeed during the speed maneuvers was approximately 21 m/s (median over all speed runs) and the average vertical wind ( $w$ ) was close to 0 (see Table S1). Yawing maneuvers were performed at an altitude ranging between 608 and 2602 m, and most  
 470 maneuvers had an average vertical wind speed close to 0 m/s (see Table S2).

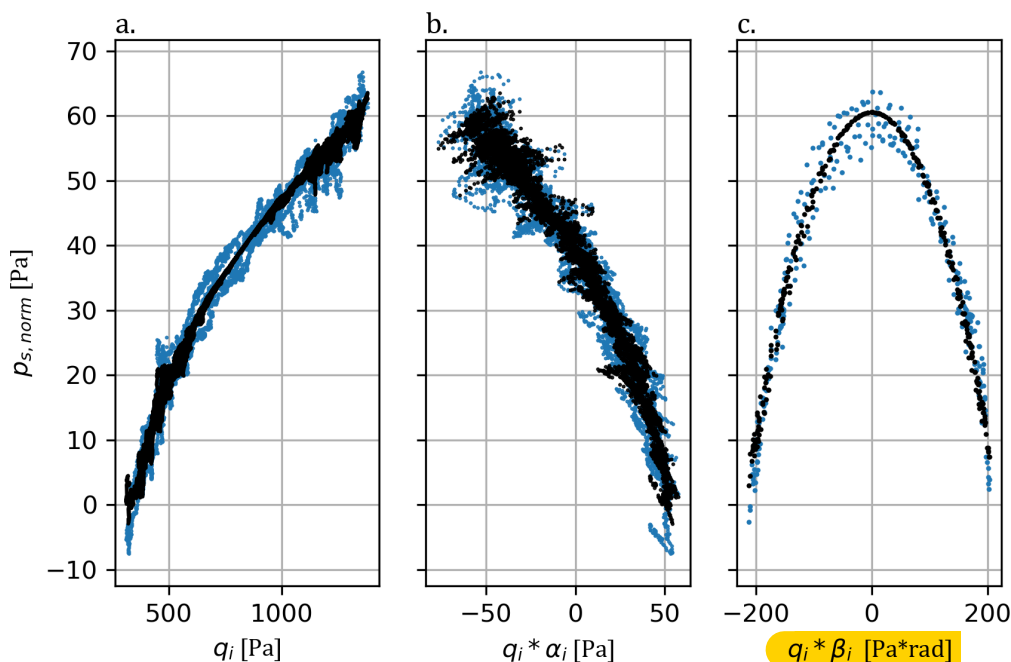


Figure 4: Example of static pressure ( $p_s$ ) calibration procedure for a calibration flight on the 7<sup>th</sup> of June, 2018. A polynomial fit is calculated for the relationship between the altitude-normalized static pressure and (a) the indicated dynamic pressure ( $p q_i$ ), (b)  $\alpha_i$  and (c)  $\beta_i$ , resulting in the following function:

$$p_{s, norm} = 0.048 * p_q - 1.98 * p_q * \alpha_i^2 - 1.25 * p_q * \beta_i^2.$$



In general, the static pressure defect could be well explained for all available maneuvers. Fig. 4 shows an exemplary calibration for a speed and a yawing maneuver flown on the 7<sup>th</sup> of June 2018. Clearly, the static pressure defect could be well explained by the variability in dynamic pressure and pressure angles  
 475 (coefficient of determination ( $r^2$ ) = 0.98 for the speed maneuver; 0.86 for the yawing maneuver). For all other maneuvers, the static pressure defect was also well explained by  $p_q$ ,  $p_\alpha$  and  $p_\beta$ , resulting in  $r^2$  values ranged between 0.91 and 0.99 for all speed maneuvers (median  $r^2$  = 0.985), and between 0.71 and 0.98 for all yawing maneuvers (median  $r^2$  = 0.97).

### 3.1.2 Dynamic Pressure

480 The dynamic pressure was calibrated with 37 reverse heading maneuvers that were performed in Germany (DE) and Czech Republic between 2017 and 2022 (for more details, see Supplement A, Table S3 and S4). In general, the average vertical wind was close to 0 and the conditions during the outbound and return flight were very similar (track length, flight time, windspeed, wind direction, wind vectors; see Table S4). Before the calibration parameter for the dynamic pressure were defined, we also checked if the average  
 485  $v_{gs}$  of each of the 37 flight pairs is similar to the average  $v_{tas}$  over both flight sections. This is crucial, as this is an important assumption for the calibration of the dynamic pressure according to Hartmann et al. (2018), specifically for Eq. 6. As shown in Fig. 5a, the relationship between  $v_{gs}$  and  $v_{tas}$  (where we account for  $\gamma$ , the difference between the true track and true heading) is located very close to the 1:1 line ( $y = 1.02x$ ). This means that flight conditions during both flight segments (outbound and return) were  
 490 very similar, and dynamic pressure could be calibrated with Eq. 4.

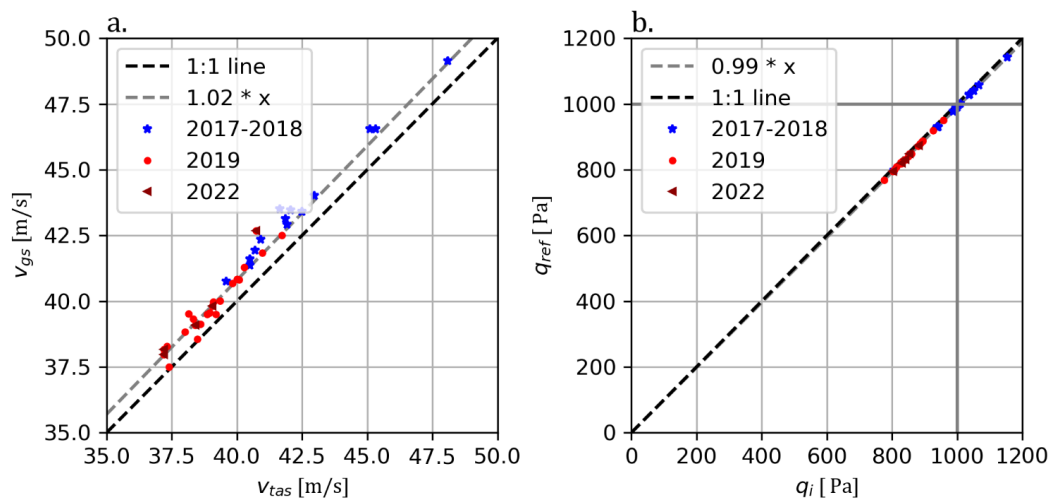




**Figure 5:** (a.) Relationship between mean  $V_{tas}$  and  $V_{gs}$  for 37 reverse heading maneuvers colored by measurement year (2017 – 2018, 2019 and 2022) (b.) Relationship between the average indicated dynamic pressure ( $q_i$ ) and the reference dynamic pressure (for 37 reverse heading maneuvers; see equations 5 and 6).

495

The results of the dynamic pressure calibration are presented in Fig. 5b. Clearly, the relationship between the average indicated dynamic pressure ( $q_i$ ) and the average reference dynamic pressure ( $q_{ref}$ ) of two overpasses is close to the 1:1 line ( $y = 0.99x$ ; see Table 3). These findings are different from Hartmann et al. (2018), who found a clear underestimation of the indicated dynamic pressure ( $c_q = 1.165$ ) as measured by the five-hole probe of the Polar 5 aircraft, showing that a correction of the dynamic pressure was required. Similar to Hartmann et al. (2018), we use the median average deviation from the regression line to estimate the accuracy of the calibration. Considering all 37 measurement flights, the median average deviation of the model residuals was 0.01 hPa, which is similar to the calibration accuracy obtained by Hartmann et al. (2018).

### 505 3.1.3 Sideslip Angle

The in-flight calibration of  $\beta$  was performed using data from nine yawing maneuvers and 37 reverse heading maneuvers that were recorded between 2017 and 2022 (for more details, see Supplement A, Table S2 – S4). Figure 6 shows an example of a sideslip angle calibration ( $C\beta$ ) for the 21<sup>st</sup> of September 2019. During the maneuver, 5 oscillations were performed and the period of each oscillation was ca. 4.2 seconds ( $\approx 0.24$  Hz). The amplitude of the maneuver was ca.  $10^\circ$  (crosswind) and the variability in the horizontal wind components after calibration was relatively small ( $\sigma(u) = 0.2$  m/s;  $\sigma(v) = 0.16$  m/s). This remaining variance of  $u$  and  $v$  followed the criterion proposed by Lenschow and Spyers-Duran (1989) and was below 10% of the induced cross wind, suggesting a successful calibration.

515 Overall, the determination of  $C\beta$  was successful, as the 10% variance criterion according to Lenschow and Spyers-Duran (1989) was fulfilled for all nine yawing maneuvers. The overall standard deviation of  $u$  and  $v$  was small for all maneuvers (median  $\sigma(u)$  and  $\sigma(v) = 0.25$  m/s), suggesting that the obtained calibration parameters can largely reduce the effects of heading changes on the horizontal wind vectors. The variability of the obtained  $C\beta$  for the entire measurement period (2017 – 2022) was very small (520 ( $\sigma(C\beta) = 0.001$ )) and resulting in very similar calibration values for 2017/2018 (median  $C\beta = 0.072$ ;  $N = 5$  maneuvers) and 2019/2022 (median  $C\beta = 0.072$ ,  $N = 4$  maneuvers). This is in agreement with Hartmann et al. (2018), who already stated that  $C\beta$  should not change over time (between different measurement campaigns).

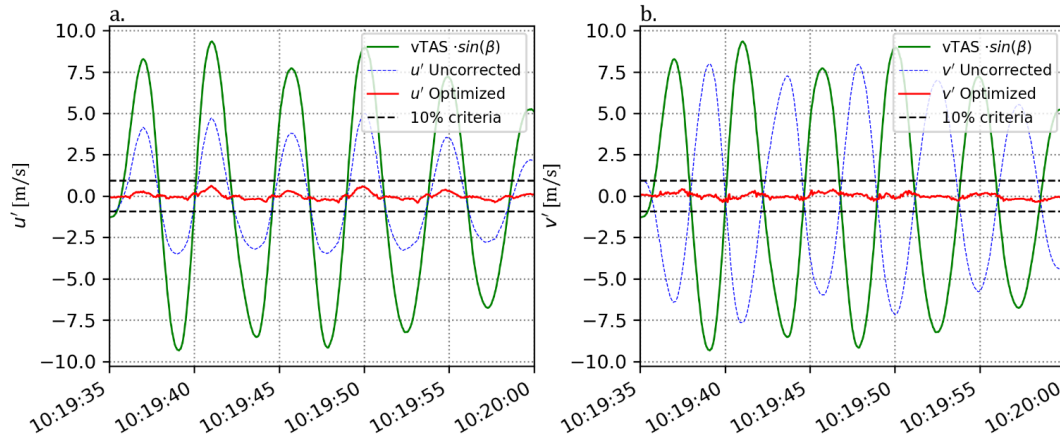


**Figure 6:** Results of sideslip angle calibration  $C_\beta$  for a yawing maneuver performed with the ASK-16 on the 21<sup>st</sup> of September 2019. During the determination of  $C_\beta$ , the standard deviation in  $u$  and  $v$  is optimized simultaneously. The blue line indicates  $u'$  (Figure a) and  $v'$  (Figure b) wind vectors with no consideration of  $C_\beta$  ( $C_\beta = 1$ ), the red line shows the optimized  $u'$  and  $v'$  wind vectors ( $C_\beta = 0.071$ ). Black striped lines indicate the maximum allowed deviation of  $u'$  and  $v'$  (10% of the induced cross wind – in green) as proposed by Lenschow and Spyers-Duran (1989),  $\sigma_u$  and  $\sigma_v$  were 0.2 m/s and 0.16 m/s respectively.

525

The offset of  $\beta$  ( $\beta_0$ ), on the other hand, is more likely to change after remounting the wingpod (Hartmann et al., 2018). The offset of  $\beta_0$  was determined with the 37 reverse heading maneuvers (see Supplement A Table S4 for details on maneuver conditions). The variability in  $\beta_0$  was the quite large (ranging between 0.49 up to -2.11), and the difference in mean  $u$  and  $v$  for the outbound and return flight ranged from small (0.01 m/s) to being substantial (1.98 m/s). These differences can also be caused by changes in local wind conditions and other flight conditions (e.g. altitude, difference in track, etc.). The differences in windspeed and wind direction are, on the other hand, acceptable, especially considering that it is impossible to have entirely similar atmospheric conditions during both legs. Overall, the average  $\beta_0$  is very similar for both calibration periods (2017/2018: -0.75, 2019/2022: -0.76) and should provide a good offset value to reduce aircraft-related differences in average horizontal wind components as much as possible. As the given pairs contain quite different meteorological conditions, the applied parameterization should be applicable to a wide range of flight conditions (while fulfilling stationarity and integral turbulence characteristics criteria).

535



### 3.1.4 Angle of Attack

540 Seven pitching maneuvers were performed between 2017 and 2022 to determine  $C_\alpha$  (for more information see Supplement A, Table S5). Figure 7 shows two examples of angle of attack calibrations for a pitching maneuver performed on the 18<sup>th</sup> of July 2018 and (b.) other maneuver that was performed on the 7<sup>th</sup> of June 2018. The amplitude of the vertical velocity of the aircraft during the pitching oscillations ranged between 7 m/s (7b) up to 15 m/s (7a) and the period of each oscillation was ca. 12.4 – 14.5 seconds. Similar to the yawing maneuvers, the variability in the vertical wind vector after calibration was relatively small ( $\sigma(w) = 0.17 - 0.27$  m/s) compared to the amplitude of the vertical velocity of the aircraft ( $w_p = 15$  m/s). The total oscillation was much smaller than the maximum allowed variation in  $w$  as proposed by Lenschow and Spyers-Duran (1989), showing that the calibration of the angle of attack was successful.

550

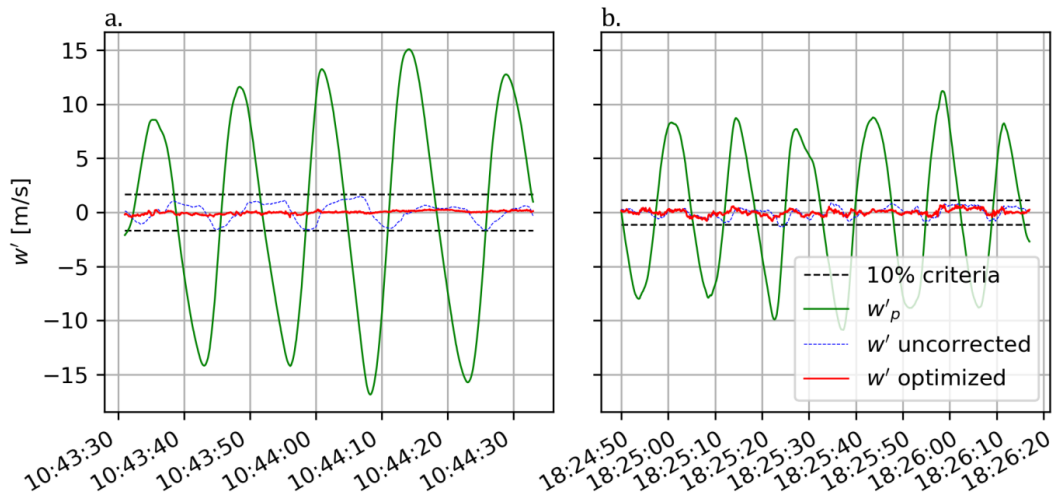


**Figure 7:** Results of the angle of attack calibration  $C_\alpha$  for a pitching maneuver performed with the ASK-16 from (a.) the 18<sup>th</sup> of July 2018 and (b.) the 7<sup>th</sup> of June 2018. The blue line indicates vertical wind speed ( $w'$ ) without any specific calibration ( $C_\alpha = 1$ , the red line shows the optimized wind vector  $w'$ , where  $C_\alpha = 0.093$ ). During the determination of  $C_\alpha$ , the standard deviation of  $w'$  is optimized. The mean vertical wind was subtracted from the measurement to better visualize the residual error in  $w$  during the pitching oscillation. Black striped lines indicate the maximum allowed deviation of  $w'$  (10% of the vertical aircraft movement  $w'_p$ ) as proposed by Lenschow and Spyers-Duran (1989).

This variation-criterion was also fulfilled for the other six flight maneuvers, resulting in small standard deviations of  $w$  during all flights (median  $\sigma(w) = 0.23$  m/s ; mean  $\sigma(w) = 0.21$  m/s). The measurement conditions (altitude, average windspeed, groundspeed and true airspeed) were variable during the



555 different pitching maneuvers, showing that the proposed  $C_\alpha$  values are applicable under different conditions (see Supplement; Table S5). At the same time,  $C_\alpha$  for all flights was very similar (2017/2018 : 0.091; 2019/2022 : 0.091), illustrating that the calibration parameters are robust. Altogether, these results show that the slope ( $C_\alpha$ ) can reduce the effects of changes in pitch angles on the calculated vertical windspeed.

560

The offset of alpha ( $\alpha_0$ ) was determined by minimizing the absolute average  $w$  for the 74 legs that were earlier used for the calibration of the dynamic pressure and the offset of beta (see Supplement; Table S3). For the entire monitoring period (2017 – 2019), the offset of  $\alpha_0$  varied between 5.20 and 7.01, which can be related to the highly variable conditions during the legs. Still, the average  $w$  for all legs was relatively close to 0 and the average  $\alpha_0$  values (2017/2018: 5.46; 2019: 5.66) should be able to correct the offset of the angle of attack ( $\alpha$ ) under quite different flight conditions.

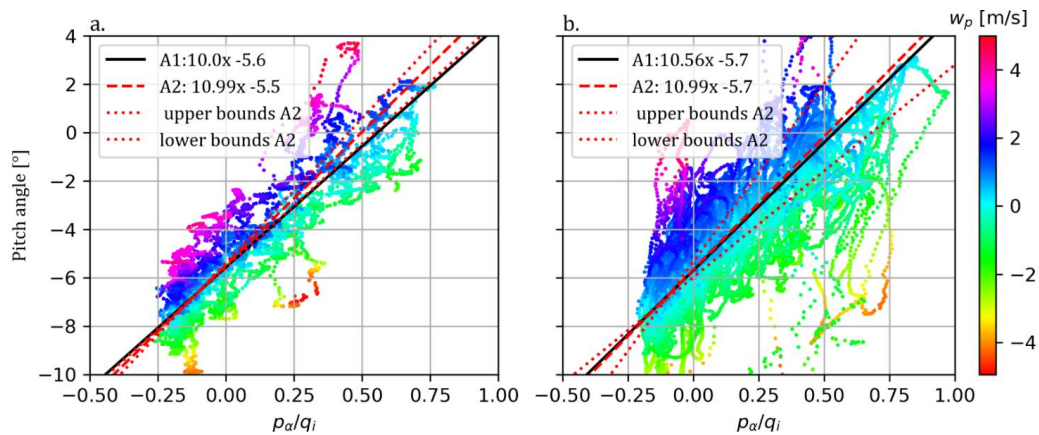


**Figure 8:** Relationship between the  $p_\alpha/q_i$  [-] and the pitch angle [°], for (a) 2017/2018 (b) and 2019/2022, color coded based on the vertical velocity of the aircraft ( $w_p$ [m/s]). The black lines present the relationship, based on a simple linear regression data where  $|w_p| < 1.5$  (represented by Eq A1). The red lines present the correction of the angle of attack based on seven pitching maneuvers and 76 flight legs (represented by Eq. A2; see Table 3).

An alternative approach to look at the correction factors for  $\alpha$ , is to look at speed runs and plot  $p_\alpha/q_i$  and the pitch angle, with respect to the vertical velocity of the aircraft  $w_p$  as proposed by Hartmann et al. (2018). Table S1 shows the speed runs that were used for the alternative calibration of  $\alpha$  (Eq A1). Figure 8 shows the relationship between  $\frac{p_\alpha}{q_i}$  and the pitch angle for all maneuvers in 2017/2018 and 2019 and 2022, including only segments where  $w_p$  was smaller than 5 m/s. Clearly, the alternative calibration based



on the speed run data ( $w_p < 1.5 \frac{m}{s}$ ; black curve) fits the data quite similarly compared to the first calibration approach (Eq. A2, red curve with uncertainty boundaries; based on pitching oscillations and straight flight legs). The fact that both methods provide quite similar calibration curves, shows that both approaches can be used to calibrate  $\alpha$ .

### 3.2 Wind Quality Evaluation

The quality of the final wind product obtained from the ASK-16 measurement flights can be assessed from different perspective, using multiple analysis results. First, we assess the quality of the wind vector based on the calibration results from the different maneuvers as presented in section 3.1. In general, the calibration results have shown that the effect of aircraft movement on the measured wind vector can be significantly reduced by the obtained calibration parameters (see Table 3). The obtained parameters seem to be robust as they show little variation during different flight conditions (wind speed, temperature, humidity, measurement altitude, etc.).

Additionally, yaw and pitch maneuvers can provide us with information about the remaining uncertainty of the wind components. Sideslip and angle of attack calibration results show that the remaining uncertainty (precision; here defined as standard deviation during pitching/yawing maneuver) of  $w$ ,  $u$  and  $v$  is in most cases between 0.2 and 0.25 m/s when the vertical speed of the aircraft is on average 0.21 m/s. Considering that the horizontal and vertical movement of the aircraft is generally much smaller during real measurement flights, the real accuracy of  $w$ ,  $u$  and  $v$  is expected to be smaller.

Another way to look at the quality of the calibration is to look at the wind vectors obtained during wind square maneuvers. Figure 9 shows uncalibrated and calibrated wind speed, wind direction (Fig. 9a and b),  $u$  and  $v$  (Fig. 9d and e) during a wind square maneuver flown on the 21<sup>st</sup> of September 2019. Here, the uncalibrated wind vectors show a clear change of  $u$  and  $v$  with the horizontal movement of the aircraft (yaw angle  $\psi$ ), indicating that the wind vectors are affected by the movement of the aircraft. This bias is not visible in the calibrated wind vector, where we see a more homogeneous wind field, and a generally smaller variability in wind speed, wind direction,  $u$ , and  $v$ . Considering that the wind calibration parameters have been obtained independently, these results show that the calibration parameters reduce aircraft movement induced effects on the wind vectors can be successfully applied to other flight data.

A third way to assess the quality of the obtained wind vectors is to assess the data in frequency space. Figure 10 shows power spectra of the calculated  $u$ ,  $v$ ,  $w$ , the measured temperature and the abundance of CH<sub>4</sub> CO<sub>2</sub> and H<sub>2</sub>O for a flight leg (ca. 26 km long) flown on the 21<sup>st</sup> of August 2019 over northeast Germany. Flight legs were flown at an altitude of 150 - 230 m.a.g.l., the wind was coming from the west and the boundary layer thickness during these flights was between 2250 and 2300 m above the surface





(see Supplement B). In Fig. 10a, we clearly see that the wind follows a  $-5/3$  drop-off, describing the energy decay of turbulent elements according to Kolmogorov's law (Foken, 2017). Similar observations were made by Metzger et al. (2012) and these results suggest that the different frequencies were appropriately represented in the measurements.

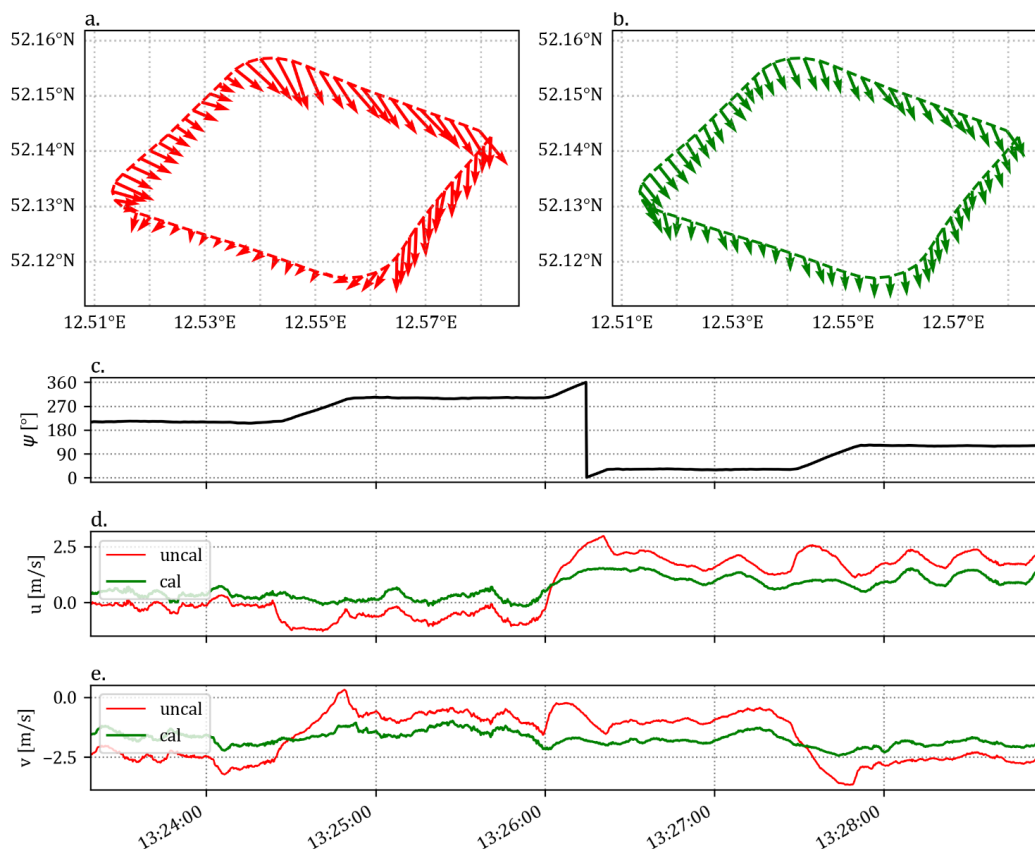


**Figure 9:** Comparing calibrated (cal; green) and uncalibrated (uncal; red) wind vectors for a wind square maneuver (duration: ca. 5.5 minutes), flown close to Bad Belzig, Germany (52.1427° N, 12.5952° E) on the 21<sup>st</sup> of September 2019. The heading as measured by the INS-GNSS (c) is plotted above both horizontal wind components  $u$  and  $v$  (subfigure d and e) to indicate the effect of the aircraft movement on the wind vector before and after calibration.

615

The spectra of the measured gasses and temperature, on the other hand, did not follow the  $-5/3$  drop-off as nicely. The observed spectral shapes indicate that these datasets contained more white noise. These results are similar to spectral analysis that were earlier reported by (Wolfe et al., 2018). Wolfe et al. (2018) and Hartmann et al. (2018), who also identified noise in the power spectra of CH<sub>4</sub> and CO<sub>2</sub> data obtained



620 from closed path LGR fast gas analyzers. However, as the white noise is generally uncorrelated to the wind data, this should not affect the obtained fluxes (see e.g. Hartmann et al., 2018). The H<sub>2</sub>O power spectrum shows clear signal attenuation (loss in signal) at higher frequencies, which is common for closed path systems (e.g. Polonik et al., 2019). This will, however, contribute to only small losses of fluxes (covariances) for the aircraft flying approximately 150 - 230 m above the surface.

625

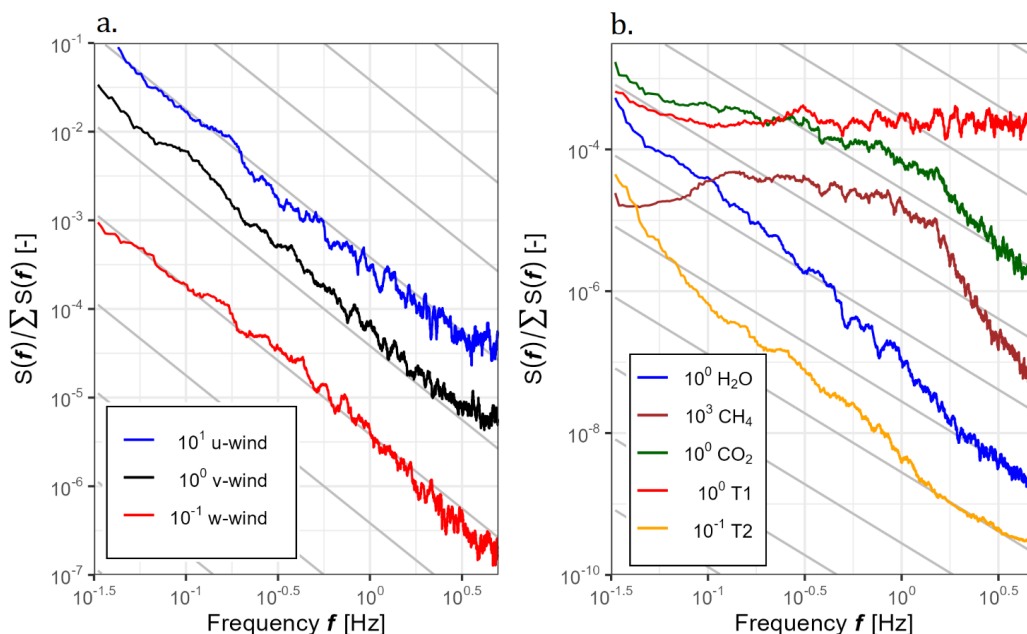


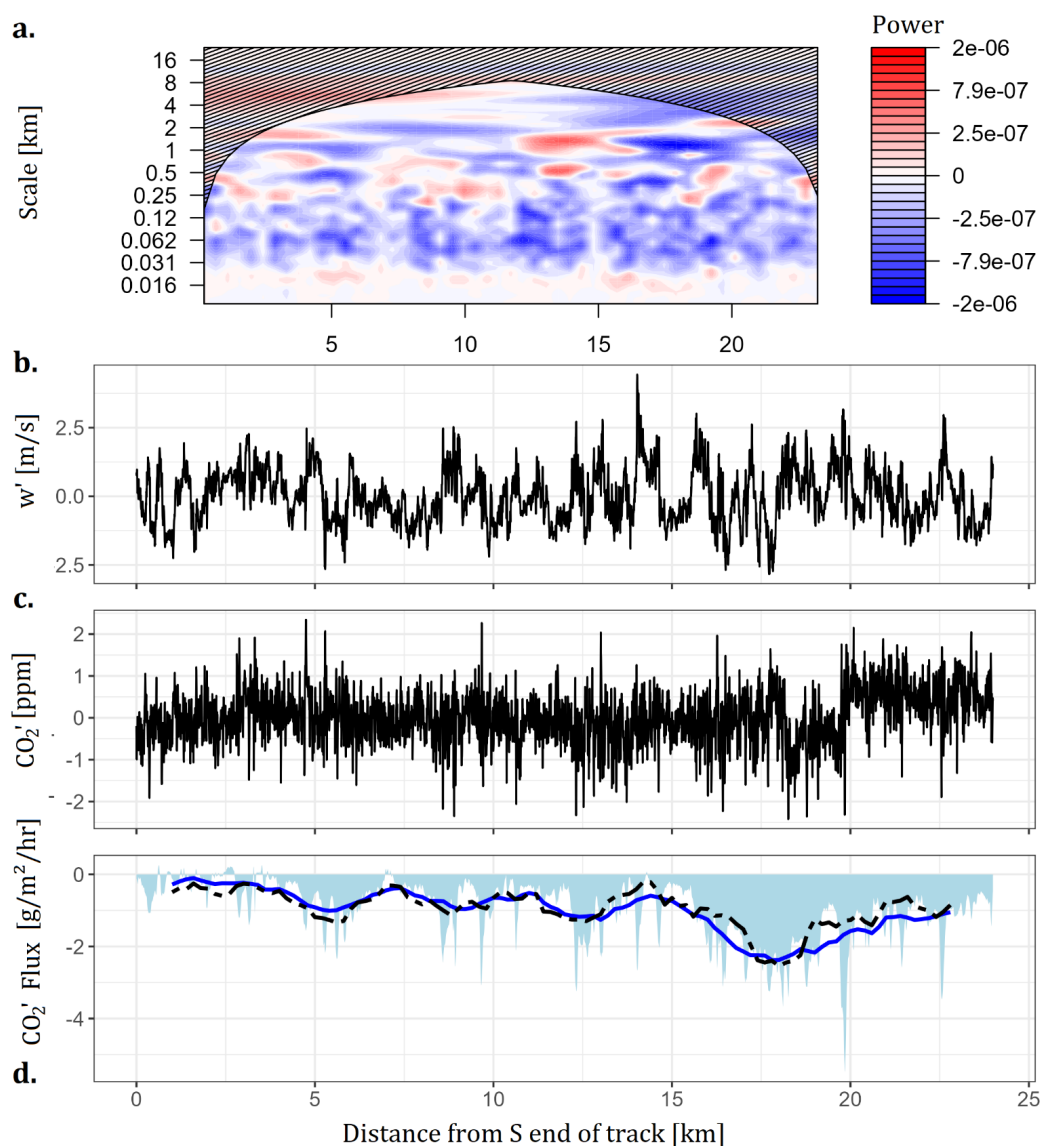
**Figure 10:** Power spectra of the fluctuations of (a) the 3-dimensional wind vector, (b) the measured gasses, and the air temperature data ( $T1 = \text{thermocouple}$ ,  $T2 = \text{Vaisala Pt100 sensor}$ ). The raw spectra are obtained from a 10-minute time series and are smoothed (“daniell” kernel from stats library in R), normalized by total spectral power and therefore non-dimensional. All straight slopes show a  $-5/3$  decrease, showing the theoretical decay of turbulence with increasing frequency according to (grey lines) Kolmogorov’s law (Foken, 2017). These power spectra show flight data from one flight leg (flight date: 21<sup>st</sup> of August 2019; altitude: between 220 and 310 m.a.s.l.) over a heterogeneous landscape (land use: mainly forest and lakes), close to the Müritz national park in Germany.

### 3.3 Fluxes and Footprints over Northeast Germany

To illustrate the flux output that was obtained with the eddy4R packages, we used flight data from 29<sup>th</sup> of August 2018 flown in the surroundings of Demmin (53.9056° N, 13.0498° E) and the Kummerower See  
 630 (53.7991° N, 12.8499° E) in Northeast Germany. During this measurement flight, five flight legs were flown over a heterogeneous transect with lake, forest, agricultural, grassland and peatland segments (Fig. 12e). Figure 11 shows exemplary wavelet and Reynolds based CO<sub>2</sub> fluxes for the first flight leg (northeast



to southwest). The dominant blue color in the cross-scalogram (Fig. 11a) reveals that we mainly measured an uptake of CO<sub>2</sub> (negative fluxes). The spatial pattern of the fluxes (Fig. 11d) are similar for the wavelet based and Reynolds based CO<sub>2</sub> fluxes, although the Reynolds based fluxes are generally somewhat smaller. This is expected, as wavelet-based fluxes contain lower-frequency information that is not present in the 2 km Reynolds based flux data. In general, the highest CO<sub>2</sub> uptake is observed during the first 6 to 10 km of the flight track, and is then decreasing until the southwestern end of the track.



640

**Figure 11:** CO<sub>2</sub> flux data for a flight leg (leg 2, see Table 4) flown over Northeast Germany (close to Demmin, Mecklenburg-Vorpommern, Germany), which was recorded on the 29<sup>th</sup> of August 2018. The



cross-scalogram (a) shows positive (red, upward fluxes) and negative covariances (blue, downward fluxes) between  $\text{CO}_2$ ' (b) and  $w$ '(c). In this case, blue colour dominates in the cross-scalogram, indicating that uptake of  $\text{CO}_2$  dominates during this flight leg at this time of the year. The final scale-integrated fluxes at high resolution (light blue area), and the 2 km integrated-fluxes (dark blue line) are shown on the bottom in comparison to Reynold decomposed fluxes (black dotted lines, calculated every 200 m for 2 km windows).

650

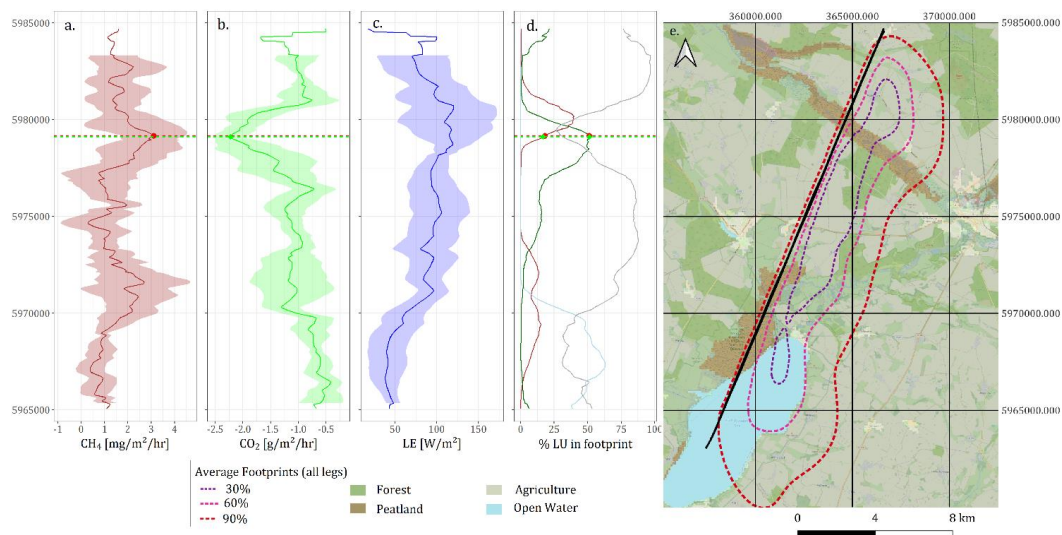


**Figure 12:** Transect with measured  $\text{CO}_2$ ,  $\text{CH}_4$  and  $\text{LE}$  (latent heat) fluxes over a heterogeneous landscape in Northeast Germany (close to Demmin; date: 29<sup>th</sup> of August 2018). The location of the transect is shown in figure 12e (background: open street maps). Flux data in graph a – c is based on airborne flight data from 5 flight legs, where thicker lines show the median fluxes and the coloured areas surrounding these lines, indicating the standard deviation of these fluxes. Besides the measured fluxes, land use cover and average footprints (based on footprints from all 5 individual legs) are shown in subfigure d and e. The land use classification presented in this map (subfigure e) is a simplified version of the Corine land cover classification of 2018 (Corine Land Cover (CLC) 2018, Version 2020\_20u1 (European Environment Agency, 2020)).

The data in Fig. 11 presents only the spatially measured  $\text{CO}_2$  flux for one flight leg. To get a broader overview of the measured fluxes, Fig. 12 shows information about the fluxes itself (a – c), their footprints (d and e) and the variability in fluxes (a-c) measured during the different flight legs. Clearly, the  $\text{CO}_2$  fluxes measured during the other flight legs were also negative, and the average spatial  $\text{CO}_2$  flux pattern was similar to the pattern already observed in Fig. 11.  $\text{CH}_4$  fluxes, on the other hand were positive and showed a mirroring trend with the largest peak in emissions in the region where the largest uptake of  $\text{CO}_2$



was observed. These peaks are connected high percentages of forest and peatland coverage. CO<sub>2</sub> uptake was largest for an area with 52.6 % of forest, 13.9 % of peatland coverage (63.5% of total coverage, green triangles in Fig. 12) and CH<sub>4</sub> fluxes were largest for an area with 50% of forest and 22% of peatland coverage (72% of total coverage, red dots in Fig. 12; according to CLC 2018, version 2020, European Environment Agency (2020)). At the same time, the highest variability in latent heat fluxes is observed in the region where the highest percentage of peatland was observed (see Fig. 12c). Figure 12 already provides a quick insight on how measured fluxes can be connected to land surface properties. Past research has already revealed that larger airborne eddy covariance datasets can have a large potential in connecting fluxes and surface properties (e.g. Metzger et al., 2013; Serafimovich et al., 2018; Vaughan et al., 2021; Zulueta et al., 2013).

### 3.4 Flux Quality Evaluation

After assessing the quality of the wind vector, the quality of the measured fluxes also needs to be evaluated. Table 4 shows the results of the stationarity assessment, the assessment of the integral turbulence characteristics, the calculated detection limits of the fluxes for the measurement flight. As a reference, the Reynolds fluxes for the entire flight legs are also provided. Mind that these fluxes do not represent the variability in the fluxes (as shown in Fig. 12), but rather the overall leg-averaged flux.

**Table 4:** Quality assessment of five flight legs flown on the 28<sup>th</sup> of August 2018, close to Demmin, Germany (see Figure 12). The table includes information about the leg-based fluxes (Reynolds Fluxes), the integral turbulence characteristics (ITCS), stationarity and the detection limits of the measured fluxes (according to Billesbach (2011)).

General		Reynolds Fluxes			ITCS			Detection Limits			Steady State	
# Flux Segments	Km covered	fLE	fCH <sub>4</sub>	fCO <sub>2</sub>	u	w	u*	LE	CH <sub>4</sub>	CO <sub>2</sub>	Stationarity test passed?	
-	km	W/m <sup>2</sup>	mg/m <sup>2</sup> /hr	g/m <sup>2</sup> /hr	%	%	%	W/m <sup>2</sup>	mg/m <sup>2</sup> /hr	g/m <sup>2</sup> /hr	-	
<b>Leg 1</b>	117	25.4	90.0	1.31	-1.31	47.6	11.4	48.7	6.2	0.52	0.12	no [CH <sub>4</sub> , CO <sub>2</sub> ]
<b>Leg 2</b>	111	24.2	79.0	1.48	-1.00	36.7	12.2	41.3	6.4	0.50	0.11	yes
<b>Leg 3</b>	112	24.4	73.8	1.99	-1.36	38.9	15.0	38.9	6.0	0.35	0.09	yes
<b>Leg 4</b>	115	25	78.7	1.63	-1.24	45.9	9.6	45.9	7.0	0.47	0.13	yes
<b>Leg 5</b>	108	23.6	128.0	1.41	-1.24	50.1	14.0	50.07	8.1	0.43	0.11	yes

665

The detection limits of the fluxes are generally much lower than the measured leg-based fluxes. Most of the 200 m based fluxes are also above these detection limits, indicating that the observed fluxes in this region are high enough to be measured with our current setup. As airborne eddy covariance fluxes can



only be measured under stationary conditions, stationarity needs to be assessed. In most case, the station-  
670 arity test was also passed, except for the first flight leg, where the stationarity requirements were not met  
for CH<sub>4</sub> and CO<sub>2</sub> fluxes. The integral turbulence characteristics are  $\leq 100\%$  for all flight segments during  
all legs, indicating that the turbulence conditions were adequate during the flight.

One way to look at the uncertainty of the calculated fluxes is to evaluate the variability in obtained fluxes  
675 for repeated flight paths. Figure 12 clearly shows the variability and therewith the uncertainty of the fluxes  
during a flight over a heterogeneous landscape indicated by the shading. The uncertainty is calculated as  
the standard deviation of five repeated measurements (flight legs) per 200 meter segment. Although part  
of the differences in fluxes might be assigned to differences in footprints, it does give an indication of the  
uncertainty of the obtained fluxes. Based on the repeated flight legs, the uncertainty in CH<sub>4</sub> fluxes was  
680  $86.2 \pm 57.7 \%$ , the uncertainty in CO<sub>2</sub> fluxes was  $32.9 \pm 12.9 \%$ , and the uncertainty in latent heat fluxes  
was  $36.6 \pm 13.0 \%$  per 200 m segment. Clearly, Fig. 12 clearly shows that even when we consider these  
uncertainties, general trends in energy and matter fluxes can still be clearly identified.

Another way to evaluate the uncertainty of the calculated fluxes is to calculate the systematic (SE) and  
685 random statistical errors (RE) according to Mann and Lenschow (1994) and Lenschow and Stankov  
(1986). Table 5 summarizes these errors both for Reynolds based and wavelet based fluxes. Larger ran-  
dom errors were generally observed for smaller CH<sub>4</sub> fluxes, which is in agreement with the observations  
by Wolfe et al., (2018). Please mind that these errors mainly describe the errors of single segments (expect  
for the relative error according to Billesbach (2011)). As we calculate a flux over a 2 km window for  
690 every 200 meters, flux segments often overlap spatially, which will decrease the error over a specific  
region. Generally, the systematic errors are very small (in most cases up to 1%) and the random errors for  
single leg segments are much larger ( $< 100\%$  for Reynolds fluxes, and  $> 100\%$  for wavelet fluxes). As  
the random shuffling method by Billesbach (2011) can also be used to determine the random error of the  
flux (e.g. Dong et al., 2021), this random flux error that is representative for a leg-averaged flux was also  
695 added to the table.

The obtained magnitudes of the systematic and random errors are similar to earlier studies (e.g. Wolfe et  
al., 2018; Metzger et al., 2012). The difference in errors between Reynolds and wavelet based fluxes can  
be explained by the fact that Mann and Lenschow (1994) assume that fluxes over a 2 km window only  
700 use fluxes within that window. This is not the case for wavelet based fluxes, where time series information  
from the entire lag is used for the derived covariances. This was already described in Wolfe et al. (2018)  
and could explain the much larger random errors for the wavelet based fluxes. The errors based on the  
repeated flight legs (Fig.12) and the Reynolds based fluxes are much more similar and are expected to be



more realistic. Overall, this suggests that random errors of individual leg segments (here 2km averaged  
705 fluxes) are rather in the range of 30-40% for LE and CO<sub>2</sub> and 80-100% for CH<sub>4</sub>.

**Table 5:** Error assessment of Airborne Fluxes for the ASK-16 platform. This table provides an overview of the systematic errors (SE) and the random errors (RE) of the calculated CO<sub>2</sub>, CH<sub>4</sub> and LE fluxes (both wavelet and Reynolds) in percentage (%). Errors were calculated according to Mann and Lenschow (1994), Lenschow and Stankov (1986), and Billesbach (2011). All flux errors are given for flight segments (a flux is calculated for a 2 km window every 200 m). The random flux error according to Billesbach (2011) was only calculated for the entire flight leg.

Leg & Flux	Segments (n)	SE Wave-let	RE Wave-let	RE Billesbach	SE Reyn-olds	RE Reyn-olds
<b>CO<sub>2</sub></b>	-	%	%	%	%	%
Leg 1 29.08.2018 CO <sub>2</sub>	117	0.9	119.1	9.2	1.0	31.8
Leg 2 29.08.2018 CO <sub>2</sub>	111	0.7	134.4	11.0	1.0	34.7
Leg 3 29.08.2018 CO <sub>2</sub>	112	0.9	108.0	6.6	0.9	29.8
Leg 4 29.08.2018 CO <sub>2</sub>	115	0.8	133.2	10.5	1.2	37.1
Leg 5 29.08.2018 CO <sub>2</sub>	108	0.8	127.5	8.9	0.9	37.8
All legs CO <sub>2</sub>	563	0.8	124.4	9.2	1.0	34.3
<b>CH<sub>4</sub></b>	-	%	%	%	%	%
Leg 1 29.08.2018 CH <sub>4</sub>	117	0.8	407.9	39.7	1.1	96.2
Leg 2 29.08.2018 CH <sub>4</sub>	111	0.6	432.5	33.8	1.0	112.9
Leg 3 29.08.2018 CH <sub>4</sub>	112	1.0	336.7	17.6	0.9	90.1
Leg 4 29.08.2018 CH <sub>4</sub>	115	0.9	397.2	28.7	1.0	97.5
Leg 5 29.08.2018 CH <sub>4</sub>	108	0.8	321.7	30.5	0.9	96.1
All legs CH <sub>4</sub>	563	0.8	379.2	30.0	1.0	98.5
<b>LE</b>	-	%	%	%	%	%
Leg 1 29.08.2018 LE	117	1.7	110.8	6.9	4.1	45.6
Leg 2 29.08.2018 LE	111	1.5	129.2	8.1	3.9	46.3
Leg 3 29.08.2018 LE	112	1.8	125.3	8.1	4.2	45.4
Leg 4 29.08.2018 LE	115	1.3	120.2	8.9	3.7	46.4
Leg 5 29.08.2018 LE	108	1.7	115.8	6.3	4.5	50.2
All legs LE	563	1.6	120.3	7.7	4.1	46.8



#### 710 **4. Conclusion and Outlook**

In this paper, we have described the ASK-16 airborne measurement platform, which can be used to measure airborne eddy covariance fluxes. Here, we have demonstrated that this platform can produce a 3-dimensional wind vector that has a similar quality as other airborne eddy covariance measurement platforms (Metzger et al., 2011; Mallaun et al., 2015; Hartmann et al., 2018). Although the spectra of the gas measurements and the fast temperature showed white noise, this should not affect fluxes as noise is uncorrelated to the measured wind (Hartmann et al., 2018). This paper has also provided a way to evaluate the quality of the obtained fluxes with the help of different tools that are available within the eddy4R toolbox, including stationarity tests, ITCS, the identification of detection limits. Detection limits for the turbulent fluxes were between 6 – 8 W/m<sup>2</sup> for LE, 0.35 – 0.52 mg/m<sup>2</sup>/hr for CH<sub>4</sub> and 0.09 – 0.13 g/m<sup>2</sup>/hr for CO<sub>2</sub>.

The flux products that can be obtained for the ASK-16 platform were illustrated using exemplary flux transects over Northeast Germany. The measurement errors of the fluxes have similar magnitudes as previously well-established airborne platforms (e.g. Metzger et al., 2012; Wolfe et al., 2018). Additionally, the flux transect data has illustrated that the ASK-16 can be used to measure turbulent fluxes over a heterogeneous landscape, such as Northeast Germany and that the obtained fluxes can be linked to surface properties. Considering the spatial distribution of eddy covariance towers and the potential of airborne platforms to cover large regions, platforms such as the ASK-16 are useful tools to bridge these scales.

#### **Acknowledgements**

730 We would like to acknowledge Hauke Dämpfling for his support in setting up the measurement system (wingpod) and creating the data logging tool. We also want to thank Jürgen Fischer and Carsten Lindemann for their (flight) support to the project. This work was funded by the Deutsche Forschungsgemeinschaft (DFG, German Research Foundation – Projektnummer 414169436 and 465048505). The National Ecological Observatory Network is a program sponsored by the National Science Foundation and operated under cooperative agreement by Battelle. This material is based in part upon work supported by the National Science Foundation through the NEON Program. We also acknowledge the support received from the NFDI4Earth Academy (Deutsche Forschungsgemeinschaft (DFG, German Research Foundation) - Projektnummer 460036893).

#### **Code availability**

740 The eddy4R v.1.3.1 software framework used to generate eddy covariance flux estimates can be freely accessed at <https://github.com/NEONScience/eddy4R> (Metzger et al., 2017). The eddy4R turbulence





v0.0.16 software module and advanced airborne data processing were accessed under terms of use (<https://www.eol.ucar.edu/content/cheesehead-code-policy-appendix>) and are available upon request. The PyWingpod source code that has been used to process the wingpod data and to calibrate the wind data of the ASK-16 is publicly available and can be accessed via <https://doi.org/10.5880/GFZ.1.4.2024.004> (Wiekenkamp et al., 2024a).

### Data availability

The data used in this manuscript is publicly available online and can be explored and downloaded via the following link: <https://doi.org/10.5880/GFZ.1.4.2024.003> (Wiekenkamp et al., 2024b).

### 750 Author contributions

IW wrote the original draft, conducted the analyses, and created the figures and tables. The conceptualization and design of this study was created by IW, TS, CW and MZ with support from JH, SM and TR. AKL and AB helped with the wind calibration procedures that are shown in the manuscript. IW, AKL, AB, JH, SM, TR, CW, MZ, TS edited and reviewed the manuscript. TR, TS provided the resources for this study and TS was responsible for the funding acquisition and project administration. Software was developed by SM (Eddy4R), IW, AKL, AB, TR, and TS (PyWingpod).

### Competing interests

The authors declare that they have no conflict of interest.

### 760 References

- Baldocchi, D. D.: Assessing the eddy covariance technique for evaluating carbon dioxide exchange rates of ecosystems: past, present and future, *Global Change Biology*, 9, 479–492, <https://doi.org/10.1046/j.1365-2486.2003.00629.x>, 2003.
- Bange, J., Spieß, T., Herold, M., Beyrich, F., and Hennemuth, B.: Turbulent fluxes from Helipod flights above quasi-homogeneous patches within the LITFASS area, *Boundary-Layer Meteorology*, 121, 127–151, 10.1007/s10546-006-9106-0, 2006.
- Billesbach, D. P.: Estimating uncertainties in individual eddy covariance flux measurements: A comparison of methods and a proposed new method, *Agricultural and Forest Meteorology*, 151, 394–405, <https://doi.org/10.1016/j.agrformet.2010.12.001>, 2011.
- Bögel, W. and Baumann, R.: Test and Calibration of the DLR Falcon Wind Measuring System by Maneuvers, *Journal of Atmospheric and Oceanic Technology*, 8, 5–18, 10.1175/1520-0426(1991)008<0005:TACOTD>2.0.CO;2, 1991.
- Chang, R. Y.-W., Miller, C. E., Dinardo, S. J., Karion, A., Sweeney, C., Daube, B. C., Henderson, J. M., Mountain, M. E., Eluszkiewicz, J., Miller, J. B., Bruhwiler, L. M. P., and Wofsy, S. C.: Methane emissions from Alaska in 2012 from CARVE airborne observations, *Proceedings of the National Academy of Sciences*, 111, 16694–16699, 10.1073/pnas.1412953111, 2014.



- Desjardins, R. L., Brach, E. J., Alvo, P., and Schuepp, P. H.: Aircraft Monitoring of Surface Carbon Dioxide Exchange, *Science*, 216, 733-735, doi:10.1126/science.216.4547.733, 1982.
- 775 Desjardins, R. L., Worth, D. E., MacPherson, J. I., Bastian, M., and Srinivasan, R.: Flux measurements by the NRC Twin Otter atmospheric research aircraft: 1987–2011, *Adv. Sci. Res.*, 13, 43-49, 10.5194/asr-13-43-2016, 2016.
- Desjardins, R. L., Worth, D. E., Pattey, E., VanderZaag, A., Srinivasan, R., Mauder, M., Worthy, D., Sweeney, C., and Metzger, S.: The challenge of reconciling bottom-up agricultural methane emissions inventories with top-down measurements, *Agricultural and Forest Meteorology*, 248, 48-59, <https://doi.org/10.1016/j.agrformet.2017.09.003>, 2018.
- 780 Dong, Y., Yang, M., Bakker, D. C. E., Kitidis, V., and Bell, T. G.: Uncertainties in eddy covariance air–sea CO<sub>2</sub> flux measurements and implications for gas transfer velocity parameterisations, *Atmos. Chem. Phys.*, 21, 8089-8110, 10.5194/acp-21-8089-2021, 2021.
- Drüe, C. and Heinemann, G.: A Review and Practical Guide to In-Flight Calibration for Aircraft Turbulence Sensors, *Journal of Atmospheric and Oceanic Technology*, 30, 2820-2837, 10.1175/JTECH-D-12-00103.1, 2013.
- 785 European Environment Agency: Corine Land Cover (CLC) 2018, Version 2020\_20u1 [dataset], <https://land.copernicus.eu/pan-european/corine-land-cover/clc2018>, 2020.
- Foken, T.: *Micrometeorology*, Springer Berlin Heidelberg, 10.1007/978-3-642-25440-6, 2017.
- Foken, T. and Wichura, B.: Tools for quality assessment of surface-based flux measurements, *Agricultural and Forest*
- 790 *Meteorology*, 78, 83-105, [https://doi.org/10.1016/0168-1923\(95\)02248-1](https://doi.org/10.1016/0168-1923(95)02248-1), 1996.
- Fortak, H.: *Messungen an Kühlturmflügen Teil 3: Dreidimensionale Vermessung von Kühlturmflügen*, 1975.
- Fortak, H.: *Messungen an Kühlturmflügen Teil 4: Ergebnisse von Meßkampagnen an den Kühltürmen der RWE-Kraftwerke Neurath und Meppen, Kernforschungsanlage Jülich*, Verlag, Jülich, Book, 290 p., 1976.
- Gioli, B., Miglietta, F., Vaccari, F. P., Zaldei, A., and Martino, B.: The Sky Arrow ERA, an innovative airborne platform to
- 795 monitor mass, momentum and energy exchange of ecosystems, *Annals of Geophysics*, 49, 10.4401/ag-3159, 2006.
- Gioli, B., Miglietta, F., Martino, B., Hutjes, R., Dolman, H., Lindroth, A., Schumacher, M., Sanz-Sanchez, M.-J., Manca, G., Peressotti, A., and Dumas, E.: Comparison between tower and aircraft-based eddy covariance fluxes in five European regions, *Agricultural and Forest Meteorology*, 127, 1-16, 10.1016/j.agrformet.2004.08.004, 2004.
- Hannun, R. A., Wolfe, G. M., Kawa, S. R., Hanisco, T. F., Newman, P. A., Alfieri, J. G., Barrick, J., Clark, K. L., DiGangi, J.
- 800 P., and Diskin, G. S.: Spatial heterogeneity in CO<sub>2</sub>, CH<sub>4</sub>, and energy fluxes: insights from airborne eddy covariance measurements over the Mid-Atlantic region, *Environ. Res. Lett.*, 15, 2020.
- Hartmann, J., Gehrman, M., Kohnert, K., Metzger, S., and Sachs, T.: New calibration procedures for airborne turbulence measurements and accuracy of the methane fluxes during the AirMeth campaigns, *Atmos. Meas. Tech.*, 11, 4567-4581, 10.5194/amt-11-4567-2018, 2018.
- 805 Högström, U.: Non-dimensional wind and temperature profiles in the atmospheric surface layer: A re-evaluation, *Boundary-Layer Meteorology*, 42, 55-78, 10.1007/BF00119875, 1988.
- Jung, M., Schwalm, C., Migliavacca, M., Walther, S., Camps-Valls, G., Koirala, S., Anthoni, P., Besnard, S., Bodesheim, P., Carvalhais, N., Chevallier, F., Gans, F., Goll, D. S., Haverd, V., Köhler, P., Ichii, K., Jain, A. K., Liu, J., Lombardozzi, D., Nabel, J. E. M. S., Nelson, J. A., O'Sullivan, M., Pallandt, M., Papale, D., Peters, W., Pongratz, J., Rödenbeck, C., Sitoh, S.,
- 810 Tramontana, G., Walker, A., Weber, U., and Reichstein, M.: Scaling carbon fluxes from eddy covariance sites to globe: synthesis and evaluation of the FLUXCOM approach, *Biogeosciences*, 17, 1343-1365, 10.5194/bg-17-1343-2020, 2020.
- Kaharabata, S. K., Schuepp, P. H., Ogunjemiyo, S., Shen, S., Leclerc, M. Y., Desjardins, R. L., and MacPherson, J. I.: Footprint considerations in BOREAS, *Journal of Geophysical Research: Atmospheres*, 102, 29113-29124, <https://doi.org/10.1029/97JD02559>, 1997.



- 815 Kalogiros, J. A. and Wang, Q.: Calibration of a Radome-Differential GPS System on a Twin Otter Research Aircraft for Turbulence Measurements, *Journal of Atmospheric and Oceanic Technology*, 19, 159-171, 10.1175/1520-0426(2002)019<0159:Coardg>2.0.Co;2, 2002.
- Karl, T., Apel, E., Hodzic, A., Riemer, D. D., Blake, D. R., and Wiedinmyer, C.: Emissions of volatile organic compounds inferred from airborne flux measurements over a megacity, *Atmos. Chem. Phys.*, 9, 271-285, 10.5194/acp-9-271-2009, 2009.
- 820 Kirby, S., Dobosy, R., Williamson, D., and Dumas, E.: An aircraft-based data analysis method for discerning individual fluxes in a heterogeneous agricultural landscape, *Agricultural and Forest Meteorology*, 148, 481-489, <https://doi.org/10.1016/j.agrformet.2007.10.011>, 2008.
- Kljun, N., Calanca, P., Rotach, M. W., and Schmid, H. P.: A Simple Parameterisation for Flux Footprint Predictions, *Boundary-Layer Meteorology*, 112, 503-523, 10.1023/B:BOUN.0000030653.71031.96, 2004.
- 825 Kohnert, K., Serafimovich, A., Metzger, S., Hartmann, J., and Sachs, T.: Strong geologic methane emissions from discontinuous terrestrial permafrost in the Mackenzie Delta, Canada, *Scientific Reports*, 7, 5828, 10.1038/s41598-017-05783-2, 2017.
- Kohnert, K., Juhls, B., Muster, S., Antonova, S., Serafimovich, A., Metzger, S., Hartmann, J., and Sachs, T.: Toward understanding the contribution of waterbodies to the methane emissions of a permafrost landscape on a regional scale—A case study from the Mackenzie Delta, Canada, *Global Change Biology*, 24, 3976-3989, <https://doi.org/10.1111/gcb.14289>, 2018.
- 830 Lehmann, A. K.: Analysis of the quality and sensitivity of the wind vector calculation towards the calibration of the ASK-16 motor glider turbulence measurement system, Department of earth sciences, institute of meteorology, radiation and remote sensing of atmospheres Freie Universitaet Berlin, Berlin, 2022.
- Lenschow, D., Delany, A., Stankov, B., and Stedman, D.: Airborne measurements of the vertical flux of ozone in the boundary layer, *Boundary-Layer Meteorology*, 19, 10.1007/BF00117223, 1980.
- 835 Lenschow, D. H. and Spyers-Duran, P.: RAF Bulletin 23: Measurement techniques: Air motion sensing (updated 2001), University Corporation for Atmospheric Research, 1989.
- Lenschow, H.: Probing the atmospheric boundary layer, American Meteorology Society Boston, MA, USA1986.
- Mallaun, C., Giez, A., and Baumann, R.: Calibration of 3-D wind measurements on a single-engine research aircraft, *Atmos. Meas. Tech.*, 8, 3177-3196, 10.5194/amt-8-3177-2015, 2015.
- 840 Mann, J. and Lenschow, D.: Errors in airborne flux measurements, *Journal of Geophysical Research*, 991, 14519-14526, 10.1029/94JD00737, 1994.
- Mauder, M., Desjardins, R., and MacPherson, J.: Scale analysis of airborne flux measurements over heterogeneous terrain in a boreal ecosystem, *Journal of Geophysical Research*, 112, D13112, doi:13110.11029/12006JD008133, 845 10.1029/2006JD008133, 2007.
- Metzger, S.: Applicability of weight-shift microlight aircraft for measuring the turbulent exchange above complex terrain. , Faculty of Biology, Chemistry and Earth Sciences, University of Bayreuth, Bayreuth, 2013.
- Metzger, S., Junkermann, W., Butterbach-Bahl, K., Schmid, H. P., and Foken, T.: Corrigendum to "Measuring the 3-D wind vector with a weight-shift microlight aircraft" published in *Atmos. Meas. Tech.*, 4, 1421–1444, 2011, *Atmos. Meas. Tech.*, 4, 850 1515-1539, 10.5194/amt-4-1515-2011, 2011.
- Metzger, S., Junkermann, W., Mauder, M., Beyrich, F., Butterbach-Bahl, K., Schmid, H. P., and Foken, T.: Eddy-covariance flux measurements with a weight-shift microlight aircraft, *Atmos. Meas. Tech.*, 5, 1699-1717, 10.5194/amt-5-1699-2012, 2012.
- Metzger, S., Durden, D., Paleri, S., Sühring, M., Butterworth, B. J., Florian, C., Mauder, M., Plummer, D. M., Wanner, L., 855 Xu, K., and Desai, A. R.: Novel approach to observing system simulation experiments improves information gain of surface-atmosphere field measurements, *Atmos. Meas. Tech.*, 14, 6929-6954, 10.5194/amt-14-6929-2021, 2021.



- Metzger, S., Durden, D., Sturtevant, C., Luo, H., Pingingtha-Durden, N., Sachs, T., Serafimovich, A., Hartmann, J., Li, J., Xu, K., and Desai, A. R.: eddy4R 0.2.0: a DevOps model for community-extensible processing and analysis of eddy-covariance data based on R, Git, Docker, and HDF5, *Geosci. Model Dev.*, 10, 3189-3206, 10.5194/gmd-10-3189-2017, 2017.
- 860 Metzger, S., Junkermann, W., Mauder, M., Butterbach-Bahl, K., Trancón y Widemann, B., Neidl, F., Schäfer, K., Wieneke, S., Zheng, X. H., Schmid, H. P., and Foken, T.: Spatially explicit regionalization of airborne flux measurements using environmental response functions, *Biogeosciences*, 10, 2193-2217, 10.5194/bg-10-2193-2013, 2013.
- O'Shea, S. J., Bauguitte, S. J. B., Gallagher, M. W., Lowry, D., and Percival, C. J.: Development of a cavity-enhanced absorption spectrometer for airborne measurements of CH<sub>4</sub> and CO<sub>2</sub>, *Atmos. Meas. Tech.*, 6, 1095-1109, 10.5194/amt-6-1095-2013, 2013a.
- O'Shea, S. J., Allen, G., Gallagher, M. W., Bauguitte, S. J. B., Illingworth, S. M., Le Breton, M., Muller, J. B. A., Percival, C. J., Archibald, A. T., Oram, D. E., Parrington, M., Palmer, P. I., and Lewis, A. C.: Airborne observations of trace gases over boreal Canada during BORTAS: campaign climatology, air mass analysis and enhancement ratios, *Atmos. Chem. Phys.*, 13, 12451-12467, 10.5194/acp-13-12451-2013, 2013b.
- 870 Polonik, P., Chan, W. S., Billesbach, D. P., Burba, G., Li, J., Nottrott, A., Bogoev, I., Conrad, B., and Biraud, S. C.: Comparison of gas analyzers for eddy covariance: Effects of analyzer type and spectral corrections on fluxes, *Agricultural and Forest Meteorology*, 272-273, 128-142, <https://doi.org/10.1016/j.agrformet.2019.02.010>, 2019.
- R Core Team: R: A Language and Environment for Statistical Computing [code], 2021.
- Rebmann, C., Aubinet, M., Schmid, H., Arriga, N., Aurela, M., Burba, G., Clement, R., De Ligne, A., Fratini, G., Gielen, B.,
- 875 Grace, J., Graf, A., Gross, P., Haapanala, S., Herbst, M., Hörtnagl, L., Ibrom, A., Joly, L., Kljun, N., Kolle, O., Kowalski, A., Lindroth, A., Loustau, D., Mammarella, I., Mauder, M., Merbold, L., Metzger, S., Mölder, M., Montagnani, L., Papale, D., Pavelka, M., Peichl, M., Roland, M., Serrano-Ortiz, P., Siebicke, L., Steinbrecher, R., Tuovinen, J.-P., Vesala, T., Wohlfahrt, G., and Franz, D.: ICOS eddy covariance flux-station site setup: a review, *International Agrophysics*, 32, 471-494, 10.1515/intag-2017-0044, 2018.
- 880 Sayres, D. S., Dobosy, R., Healy, C., Dumas, E., Kochendorfer, J., Munster, J., Wilkerson, J., Baker, B., and Anderson, J. G.: Arctic regional methane fluxes by ecotope as derived using eddy covariance from a low-flying aircraft, *Atmos. Chem. Phys.*, 17, 8619-8633, 10.5194/acp-17-8619-2017, 2017.
- Serafimovich, A., Metzger, S., Hartmann, J., Kohnert, K., Zona, D., and Sachs, T.: Upscaling surface energy fluxes over the North Slope of Alaska using airborne eddy-covariance measurements and environmental response functions, *Atmos. Chem.*
- 885 *Phys.*, 18, 10007-10023, 10.5194/acp-18-10007-2018, 2018.
- Sun, Y., Sude, B., Geng, B., Ma, J., Lin, X., Hao, Z., Jing, W., Chen, Q., and Quan, Z.: Observation of the winter regional evaporative fraction using a UAV-based eddy covariance system over wetland area, *Agricultural and Forest Meteorology*, 310, 108619, <https://doi.org/10.1016/j.agrformet.2021.108619>, 2021.
- Tetzlaff, A., Lüpkes, C., and Hartmann, J.: Aircraft-based observations of atmospheric boundary-layer modification over
- 890 Arctic leads, *Quarterly Journal of the Royal Meteorological Society*, doi:10.1002/qj.2568, 2015.
- Thomas, C. and Foken, T.: Re-evaluation of Integral Turbulence Characteristics and their Parameterisations, 15th Conference on Boundary Layer and Turbulence, Wageningen, the Netherlands,
- Tjernström, M. and Friehe, C.: Analysis of a Radome Air-Motion System on a Twin-Jet Aircraft for Boundary-Layer Research, *Journal of Atmospheric and Oceanic Technology*, 8, 19-40, 10.1175/1520-0426(1991)008<0019:AOARAM>2.0.CO;2, 1991.
- 895 Torrence, C. and Compo, G. P.: A Practical Guide to Wavelet Analysis, *Bulletin of the American Meteorological Society*, 79, 61-78, [https://doi.org/10.1175/1520-0477\(1998\)079<0061:APGTWA>2.0.CO;2](https://doi.org/10.1175/1520-0477(1998)079<0061:APGTWA>2.0.CO;2), 1998.
- Vaughan, A. R., Lee, J. D., Metzger, S., Durden, D., Lewis, A. C., Shaw, M. D., Drysdale, W. S., Purvis, R. M., Davison, B., and Hewitt, C. N.: Spatially and temporally resolved measurements of NO<sub>x</sub> fluxes by airborne eddy covariance over Greater London, *Atmos. Chem. Phys.*, 21, 15283-15298, 10.5194/acp-21-15283-2021, 2021.



- 900 Vaughan, A. R., Lee, J. D., Misztal, P. K., Metzger, S., Shaw, M. D., Lewis, A. C., Purvis, R. M., Carslaw, D. C., Goldstein, A. H., Hewitt, C. N., Davison, B., Beevers, S. D., and Karl, T. G.: Spatially resolved flux measurements of NO<sub>x</sub> from London suggest significantly higher emissions than predicted by inventories, *Faraday Discussions*, 189, 455-472, 10.1039/C5FD00170F, 2016.
- Vaughan, A. R., Lee, J. D., Shaw, M. D., Misztal, P. K., Metzger, S., Vieno, M., Davison, B., Karl, T. G., Carpenter, L. J., Lewis, A. C., Purvis, R. M., Goldstein, A. H., and Hewitt, C. N.: VOC emission rates over London and South East England obtained by airborne eddy covariance, *Faraday Discussions*, 200, 599-620, 10.1039/C7FD00002B, 2017.
- 905 Vellinga, O. S., Dobosy, R. J., Dumas, E. J., Gioli, B., Elbers, J. A., and Hutjes, R. W. A.: Calibration and Quality Assurance of Flux Observations from a Small Research Aircraft, *Journal of Atmospheric and Oceanic Technology*, 30, 161-181, 10.1175/JTECH-D-11-00138.1, 2013.
- 910 Vickers, D. and Mahrt, L.: Quality Control and Flux Sampling Problems for Tower and Aircraft Data, *Journal of Atmospheric and Oceanic Technology*, 14, 512-526, 10.1175/1520-0426(1997)014<0512:QCAFSP>2.0.CO;2, 1997.
- Vihma, T. and Kottmeier, C.: A Modelling Approach For Optimizing Flight Patterns In Airborne Meteorological Measurements, *Boundary-Layer Meteorology*, 95, 211-230, 10.1023/A:1002634613282, 2000.
- Virtanen, P., Gommers, R., Oliphant, T. E., Haberland, M., Reddy, T., Cournapeau, D., Burovski, E., Peterson, P., Weckesser, W., Bright, J., van der Walt, S. J., Brett, M., Wilson, J., Millman, K. J., Mayorov, N., Nelson, A. R. J., Jones, E., Kern, R., Larson, E., Carey, C. J., Polat, İ., Feng, Y., Moore, E. W., VanderPlas, J., Laxalde, D., Perktold, J., Cimrman, R., Henriksen, I., Quintero, E. A., Harris, C. R., Archibald, A. M., Ribeiro, A. H., Pedregosa, F., van Mulbregt, P., Vijaykumar, A., Bardelli, A. P., Rothberg, A., Hilboll, A., Kloeckner, A., Scopatz, A., Lee, A., Rokem, A., Woods, C. N., Fulton, C., Masson, C., Häggström, C., Fitzgerald, C., Nicholson, D. A., Hagen, D. R., Pasechnik, D. V., Olivetti, E., Martin, E., Wieser, E., Silva, F., 915 Lenders, F., Wilhelm, F., Young, G., Price, G. A., Ingold, G.-L., Allen, G. E., Lee, G. R., Audren, H., Probst, I., Dietrich, J. P., Silterra, J., Webber, J. T., Slavič, J., Nothman, J., Buchner, J., Kulick, J., Schönberger, J. L., de Miranda Cardoso, J. V., Reimer, J., Harrington, J., Rodríguez, J. L. C., Nunez-Iglesias, J., Kuczynski, J., Tritz, K., Thoma, M., Newville, M., Kümmerer, M., Bolingbroke, M., Tartre, M., Pak, M., Smith, N. J., Nowaczyk, N., Shebanov, N., Pavlyk, O., Brodtkorb, P. A., Lee, P., McGibbon, R. T., Feldbauer, R., Lewis, S., Tygier, S., Sievert, S., Vigna, S., Peterson, S., More, S., Pudlik, T., 920 Oshima, T., Pingel, T. J., Robitaille, T. P., Spura, T., Jones, T. R., Cera, T., Leslie, T., Zito, T., Krauss, T., Upadhyay, U., Halchenko, Y. O., Vázquez-Baeza, Y., and SciPy, C.: SciPy 1.0: fundamental algorithms for scientific computing in Python, *Nature Methods*, 17, 261-272, 10.1038/s41592-019-0686-2, 2020.
- Wiekenkamp, I., Lehmann, A. K., Buetow, A., Ruhtz, T., and Sachs, T.: PyWingpod, GFZ Data Services, <https://doi.org/10.5880/GFZ.1.4.2024.004>, 2024a.
- 930 Wiekenkamp, I., Lehmann, A. K., Buetow, A., Fischer, J., Hartmann, J., Metzger, S., Ruhtz, T., Wille, C., Mathias, Z., and Sachs, T.: Airborne Wind and Eddy Covariance Dataset - Recorded with the ASK-16 EC Platform between 2017 – 2022, GFZ Data Services [dataset], <https://doi.org/10.5880/GFZ.1.4.2024.003>, 2024b.
- Williams, A. and Marcotte, D.: Wind Measurements on a Maneuvering Twin-Engine Turboprop Aircraft Accounting for Flow Distortion, *Journal of Atmospheric and Oceanic Technology*, 17, 795-810, 10.1175/1520-0426(2000)017<0795:WMOAMT>2.0.CO;2, 2000.
- 935 Wolfe, G. M., Kawa, S. R., Hanisco, T. F., Hannun, R. A., Newman, P. A., Swanson, A., Bailey, S., Barrick, J., Thornhill, K. L., Diskin, G., DiGangi, J., Nowak, J. B., Sorenson, C., Bland, G., Yungel, J. K., and Swenson, C. A.: The NASA Carbon Airborne Flux Experiment (CARAFE): instrumentation and methodology, *Atmos. Meas. Tech.*, 11, 1757-1776, 10.5194/amt-11-1757-2018, 2018.
- 940 Xu, K., Metzger, S., and Desai, A. R.: Upscaling tower-observed turbulent exchange at fine spatio-temporal resolution using environmental response functions, *Agricultural and Forest Meteorology*, 232, 10-22, <https://doi.org/10.1016/j.agrformet.2016.07.019>, 2017.



- Yuan, B., Kaser, L., Karl, T., Graus, M., Peischl, J., Campos, T. L., Shertz, S., Apel, E. C., Hornbrook, R. S., Hills, A., Gilman, J. B., Lerner, B. M., Warneke, C., Flocke, F. M., Ryerson, T. B., Guenther, A. B., and de Gouw, J. A.: Airborne flux  
945 measurements of methane and volatile organic compounds over the Haynesville and Marcellus shale gas production regions, *Journal of Geophysical Research: Atmospheres*, 120, 6271-6289, <https://doi.org/10.1002/2015JD023242>, 2015.
- Zona, D., Gioli, B., Commane, R., Lindaas, J., Wofsy, S. C., Miller, C. E., Dinardo, S. J., Dengel, S., Sweeney, C., Karion, A., Chang, R. Y. W., Henderson, J. M., Murphy, P. C., Goodrich, J. P., Moreaux, V., Liljedahl, A., Watts, J. D., Kimball, J. S., Lipson, D. A., and Oechel, W. C.: Cold season emissions dominate the Arctic tundra methane budget, *Proceedings of the  
950 National Academy of Sciences*, 113, 40, 10.1073/pnas.1516017113, 2016.
- Zulueta, R. C., Oechel, W. C., Loescher, H. W., Lawrence, W. T., and Paw U, K. T.: Aircraft-derived regional scale CO<sub>2</sub> fluxes from vegetated drained thaw-lake basins and interstitial tundra on the Arctic Coastal Plain of Alaska, *Global Change Biology*, 17, 2781-2802, <https://doi.org/10.1111/j.1365-2486.2011.02433.x>, 2011.
- Zulueta, R. C., Oechel, W. C., Verfaillie, J. G., Hastings, S. J., Gioli, B., Lawrence, W. T., and Paw U, K. T.: Aircraft Regional-  
955 Scale Flux Measurements over Complex Landscapes of Mangroves, Desert, and Marine Ecosystems of Magdalena Bay, Mexico, *Journal of Atmospheric and Oceanic Technology*, 30, 1266-1294, 10.1175/JTECH-D-12-00022.1, 2013.

## Supplement to:

# The ASK-16 Motorized Glider: An Airborne Eddy Covariance Platform to measure Turbulence, Energy and Matter Fluxes

5

Inge Wiekenkamp<sup>1</sup>, Anna Katharina Lehmann<sup>2</sup>, Alexander Buetow<sup>2</sup>, Jürgen Fischer<sup>2</sup>, Jörg Hartmann<sup>3</sup>, Stefan Metzger<sup>4</sup>, Thomas Ruhtz<sup>2</sup>, Christian Wille<sup>1</sup>, Mathias Zöllner<sup>1</sup>, Torsten Sachs<sup>1</sup>

*Correspondence to:* Inge Wiekenkamp ([inge.wiekenkamp@gfz-potsdam.de](mailto:inge.wiekenkamp@gfz-potsdam.de))

The aim of this supplementary material is to provide transparent and detailed background information  
10 about the ASK 16 measurement platform. In supplement A more details are provided about the flight  
maneuvers that have been used to calibrate the wind measurements. This includes detailed tables, that  
present measurement conditions during the calibration maneuvers. In Supplement B more information  
about atmospheric boundary layer height conditions is given for two specific flight dates (29.08.2018 and  
21.09.2019).

## 15 **Supplement A: Flight Maneuver Information**

Flight maneuvers were performed during several calibration and measurement flights to obtain calibration parameters for the angle of attack, the sideslip angle, the static pressure and the dynamic pressure. Tables S1 – S5 provide information about flight itself (e.g. height, flight time etc.) and the meteorological conditions that were prone during the flight maneuvers. Additionally, all tables provide information about

20 the optimized parameterization of the individual flight maneuvers.



25 Table S1: General information about the speed maneuvers, including general flight information (date, time, mean height, and mean groundspeed), meteorological conditions (median windspeed, wind directions, and wind vector information). The table also includes the range in measured static pressure ( $P_s$ ) and static pressure defect (err  $P_s$ ). Wind conditions were calculated with the median calibration parameters for 2017/2018 and 2019/2022 from Table 3 (and not with the obtained calibration parameters for each individual maneuver –  $a_1$  and  $a_2$  Eq. 2). Symbology:

30  $M$  = median,  $lon$  = longitude;  $lat$  = latitude;  $alt$  = altitude;  $m.a.g.l.$  = meters above ground level;  $T$  = temperature;  $wspd$  = windspeed;  $wdir$  = wind direction,  $v_{gs}$  = groundspeed,  $r^2$  = coefficient of determination representing fit for parameters  $a_1$  and  $a_2$  (fit for parameter  $a_3$  is provided in Table S2).

<i>no</i>	<i>flight date</i>	<i>flight time</i>	<i>M(lon)</i>	<i>M(lat)</i>	<i>M(alt)</i>	<i>M(T)</i>	<i>M(wspd)</i>	<i>M(wdir)</i>	<i>M(w)</i>	<i>range</i> <i>v<sub>gs</sub></i>	<i>a<sub>1</sub></i> <i>Eq. 2</i>	<i>a<sub>2</sub></i> <i>Eq. 2</i>	<i>r<sup>2</sup> fit</i> <i>Eq</i> <i>.2</i>
	-	<i>start - end</i>	<i>deg</i>	<i>deg</i>	<i>m.a.g.l.</i>	<i>°K</i>	<i>m/s</i>	<i>°</i>	<i>m/s</i>	<i>m/s</i>	-	-	-
1	8/9/2017	17:09:54 - 17:12:46	12.516	52.1	2557	278	11.8	230	0.48	12.1 - 32.96	0.045	-2.04	0.97
2	9/21/2019	10:51:22 - 10:53:02	12.507	52.08	1052	287	2.1	318	0.05	27.28 - 48.19	0.045	-1.72	0.99
3	5/4/2022	12:28:44 - 12:29:45	12.56	52.12	779	284	2.7	135	0.49	20.93 - 48.75	0.056	-1.62	0.98
4	6/7/2018	18:12:33 - 18:18:46	12.671	52.12	631	295	7.0	112	0.05	30.19 - 57.67	0.048	-1.98	0.98
5	4/17/2019	11:08:58 - 11:20:28	12.756	51.98	1631	276	8.5	126	-0.06	18.26 - 41.51	0.047	-2.24	0.92
6	9/21/2019	10:02:39 - 10:08:56	12.406	52.01	1080	287	1.5	299	0	27.21 - 48.48	0.049	-2.09	0.94
7	9/21/2019	10:47:46 - 10:53:02	12.484	52.05	1039	287	2.0	303	0.06	27.28 - 50.1	0.046	-2.12	0.91
8	9/21/2019	10:07:11 - 10:09:56	12.345	51.98	1102	287	1.1	306	-0.05	27.73 - 47.86	0.058	-1.94	1.00
9	9/21/2019	10:09:56 - 10:13:28	12.251	51.95	1124	287	1.8	337	0.05	27.88 - 47.79	0.040	-2.42	0.99
10	9/21/2019	10:11:26 - 10:13:28	12.231	51.94	1126	287	2.0	338	-0.01	28.99 - 47.79	0.040	-2.44	0.99
11	9/21/2019	10:47:46 - 10:49:33	12.457	52.01	1047	287	1.9	294	-0.04	27.41 - 47.97	0.040	-2.15	0.99
12	9/21/2019	10:49:33 - 10:51:22	12.485	52.05	1027	287	2.1	292	0.12	27.57 - 50.1	0.053	-1.72	0.99

Table S2: General information about the performed yawing maneuvers, including general flight information (date, time height, groundspeed), meteorological conditions (windspeed, wind directions, and wind vector information) and the obtained calibration parameters – Par  $a_3$  for Eq. 2. and  $C_\beta$  for Eq. 6. All wind parameters were calculated after calibration (using median calibration values for 2017/2018 and 2019/2022 from Table 3 - and not with the parameters in the last column). Symbology:  $M$  = median;  $lat$  = latitude;  $lon$  = longitude;  $alt$  = altitude;  $m.a.g.l.$  = meters above ground level;  $T$  = temperature;  $\mu$  = average conditions;  $wspd$  = windspeed;  $wdir$  = wind direction;  $v_{gs}$  = groundspeed;  $\theta$  = Pitch angle;  $\Psi$  = heading,  $r^2$  = coefficient of determination representing fit for parameter  $a_3$  in Eq. 2 (fit for other parameters is provided in Table S1). The second part of this table is positioned on the next page.

45

Table S2 part A

<i>no</i>	<i>flight date</i>	<i>flight time</i>	<i>M(lon)</i>	<i>M(lat)</i>	<i>M(alt)</i>	<i>M(T)</i>	<i>M(wspd)</i>	<i>M(wdir)</i>	<i>M(u)</i>	$\sigma(u)$	$\sigma(v)$
	<i>yyyy-mm-dd</i>	<i>hh:mm:ss</i>	<i>deg</i>	<i>deg</i>	<i>m.a.g.l.</i>	$^{\circ}K$	<i>m/s</i>	$^{\circ}$	<i>m/s</i>	<i>m/s</i>	<i>m/s</i>
1	2017-08-09	17:07:31 - 17:07:52	12.572	52.137	2602	278.8	13.26	228.7	9.98	0.21	0.18
2	2022-06-14	10:04:40 - 10:05:25	13.462	53.351	2364	273.5	13.29	315.7	9.28	0.1	0.15
3	2018-07-16	14:44:18 - 14:44:33	13.254	52.235	606	294.2	3.04	39.2	-1.76	0.55	0.43
4	2018-07-18	10:41:46 - 10:42:48	12.462	52.188	2357	280	8.37	300.6	7.19	0.39	0.28
5	2018-07-18	10:45:19 - 10:45:46	12.521	52.207	2415	279.4	7.87	305.4	6.4	0.25	0.26
6	2018-06-07	18:26:47 - 18:27:55	12.712	52.079	630	295.2	6.12	114.5	-5.56	0.23	0.25
7	2019-04-17	11:27:58 - 11:28:40	12.666	52.03	1822	274.2	7.44	143.5	-4.28	0.38	0.55
8	2019-09-21	10:19:35 - 10:20:00	12.342	51.963	1119	286.8	1.69	300.4	1.44	0.2	0.16
9	2019-09-21	10:56:30 - 10:57:22	12.554	52.172	1038	286.8	1.83	297.5	1.59	0.37	0.25

50

55

60

Table S2 part B

<i>no</i>	<i>flight_date</i>	<i>min(g<sub>s</sub>)</i>	<i>max(g<sub>s</sub>)</i>	$\sigma(\theta)$	$\sigma(\Psi)$	$a_3 Eq. 2$	$r^2 Eq. 2$	$C\beta$	<i>Period</i>	<i>M(w)</i>	<i>M(v)</i>
	yyyy-mm-dd	m/s	m/s	°	°	-	-	-	s	m/s	m/s
1	2017-08-09	28.11	33.09	0.13	0.32	-1.02	0.71	0.072	3.01	1	8.78
2	2022-06-14	27.17	31.82	0.09	0.59	-1.50	0.94	0.070	4.10	0.32	-9.51
3	2018-07-16	43.84	46.68	0.1	0.57	-1.25	0.97	0.071	3.76	-1.2	-2.33
4	2018-07-18	25.07	31.41	0.17	0.6	-1.40	0.98	0.070	5.17	0.26	-4.29
5	2018-07-18	36.56	40.61	0.15	0.61	-1.49	0.98	0.070	5.41	0.15	-4.53
6	2018-06-07	34.47	39.92	0.09	0.45	-1.23	0.86	0.072	7.56	-0.1	2.53
7	2019-04-17	40.68	46.76	0.11	0.68	-1.72	0.97	0.069	6.01	0.53	5.94
8	2019-09-21	34.95	40.97	0.19	0.53	-1.64	0.97	0.071	4.17	0.19	-0.85
9	2019-09-21	36.3	41.44	0.1	0.61	-1.52	0.97	0.072	5.78	0.01	-0.78

65 Table S3: General information about the **unbound** and return flights (legs), including general flight information (date, flight time, height, groundspeed, true airspeed), meteorological conditions (windspeed, wind directions, and wind vector information), and information about the position of the aircraft (true track, heading and drift angle). All wind parameters were calculated after calibration (using median calibration values for 2017/2018 and 2019/2022). Symbology: *lon* = longitude, *lat* = latitude; *T* = temperature; *M* = median; *wspd* = windspeed; *wdir* = wind direction;  $v_{gs}$  = groundspeed;  $v_{tas}$  = true airspeed;  $\theta$  = Pitch angle;  $\Psi$  = Heading,

	<i>flight date</i>	<i>flight leg</i>	<i>flight time</i>	<i>dist</i>	<i>M(lon)</i>	<i>M(lat)</i>	<i>M(alt)</i>	<i>M(T)</i>	<i>M(wspd)</i>	<i>M(wdir)</i>	<i>M(<math>\gamma</math>)</i>	<i>M(w)</i>	<i>M(gs)</i>	<i>ao</i>
	<i>d/m/y</i>	-	<i>h:m:s</i>	<i>km</i>	<i>deg</i>	<i>deg</i>	<i>m.a.g.l.</i>	$^{\circ}K$	<i>m/s</i>	$^{\circ}$	$^{\circ}$	<i>m/s</i>	<i>m/s</i>	-
1	8/14/2017	Leg1	11:28:20	24.11	12.897	53.888	197	290.8	2.2	195.1	33.0	-0.33	39.6	5.20
			-											
			11:37:40											
2	8/14/2017	Leg10	16:07:00	20.34	12.899	53.91	2094	277	6.1	208.5	213.3	0.03	26.2	5.51
			-											
			16:16:00											
3	8/14/2017	Leg10	16:07:00	20.34	12.899	53.91	2094	277	6.1	208.5	213.3	0.03	26.2	5.51
			-											
			16:16:00											
4	8/14/2017	Leg1	11:28:20	24.11	12.897	53.888	197	290.8	2.2	195.1	33.0	-0.33	39.6	5.20
			-											
			11:37:40											
5	8/14/2017	Leg2	11:39:50	23.91	12.897	53.888	221	291.4	1.8	196.2	213.5	-0.26	34.15	5.36
			-											
			11:50:00											
6	8/14/2017	Leg3	11:51:00	23.95	12.897	53.89	197	291.9	2.1	202.7	33.2	-0.24	38.67	5.45
			-											
			12:00:10											
7	8/14/2017	Leg4	12:01:45	23.68	12.897	53.89	210	292	1.9	203.7	213.1	-0.18	29.52	5.48
			-											
			12:12:12											
8	8/14/2017	Leg5	10:53:00	24.26	12.913	53.894	2256	278.8	5.7	211.6	33.2	-0.04	40.24	5.46
			-											
			11:02:05											
9	8/14/2017	Leg6	11:03:05	24.22	12.892	53.899	2272	278.6	5.1	217.1	213.4	0.03	34.05	5.49
			-											
			11:14:00											
10	8/14/2017	Leg7	16:37:30	22.65	12.902	53.897	222	292.4	2.7	119.5	32.9	-0.07	37.26	5.45
			-											
			16:46:30											
11	8/14/2017	Leg8	16:48:45	23.07	12.901	53.894	229	293	2.8	83.3	213.1	0.03	39.85	5.63
			-											
			16:57:45											
12	8/14/2017	Leg9	15:57:30	22.66	12.91	53.889	1916	278.2	6.1	201.5	32.9	0.07	45.25	5.57
			-											
			16:05:20											
13	8/15/2017	Leg1	06:09:20	23.45	12.903	53.897	240	290.8	14.3	159.4	32.8	0.12	42.09	5.68
			-											
			06:17:40											
14	8/15/2017	Leg10	09:24:35	20.8	12.864	53.981	227	294	8.3	136.9	113.5	-0.11	27.79	5.45
			-											
			09:34:30											
15	8/15/2017	Leg11	10:41:30	22.54	12.91	53.89	2008	283.2	8.0	224.6	32.9	0.02	52.01	5.47
			-											
			10:48:15											
16	8/15/2017	Leg12	10:49:40	22.16	12.888	53.894	2019	283	8.3	226.4	212.8	-0.02	36.12	5.47
			-											
			10:58:50											

	<i>flight date</i>	<i>flight leg</i>	<i>flight time</i>	<i>dist</i>	<i>M(lon)</i>	<i>M(lat)</i>	<i>M(alt)</i>	<i>M(T)</i>	<i>M(wspd)</i>	<i>M(wdir)</i>	<i>M(<math>\chi</math>)</i>	<i>M(w)</i>	<i>M(gs)</i>	<i><math>\alpha_0</math></i>
	<i>d/m/y</i>	-	<i>h:m:s</i>	<i>km</i>	<i>deg</i>	<i>deg</i>	<i>m.a.g.l.</i>	$^{\circ}K$	<i>m/s</i>	$^{\circ}$	$^{\circ}$	<i>m/s</i>	<i>m/s</i>	-
17	8/15/2017	Leg2	06:20:00	23.33	12.903	53.898	249	291	12.7	155.6	213.0	-0.11	27.83	5.36
			-											
			06:32:10											
18	8/15/2017	Leg3	05:31:00	23.41	12.914	53.895	2133	281.5	3.9	231.2	33.2	-0.05	45.48	5.41
			-											
			05:39:10											
19	8/15/2017	Leg4	05:42:00	23.03	12.891	53.898	2167	281	3.2	238.9	212.9	0	40.08	5.46
			-											
			05:50:55											
20	8/15/2017	Leg5	08:36:45	23.47	12.901	53.894	217	293.2	8.1	139.1	33.2	-0.11	39.38	5.44
			-											
			08:45:40											
21	8/15/2017	Leg6	08:47:30	23.25	12.901	53.895	218	293.5	7.9	133.6	213.2	-0.08	32.12	5.45
			-											
			08:57:50											
22	8/15/2017	Leg7	09:36:45	20.14	12.868	53.979	262	294	9.0	137.8	293.5	-0.14	46.77	5.39
			-											
			09:43:30											
23	8/15/2017	Leg8	09:46:20	20.11	12.866	53.98	222	294.6	8.3	138.4	113.5	0	29.87	5.55
			-											
			09:56:00											
24	8/15/2017	Leg9	09:15:00	20.55	12.862	53.982	216	293.8	9.2	134.2	294.3	-0.08	45.47	5.42
			-											
			09:21:50											
25	8/29/2018	Leg1	12:22:58	22.55	12.904	53.899	208	294.8	6.4	139.4	213.3	-0.04	35.42	5.40
			-											
			12:32:46											
26	8/29/2018	Leg2	12:34:35	22.37	12.904	53.899	178	295.2	7.3	139.5	33.2	-0.27	41.31	5.22
			-											
			12:42:50											
27	8/29/2018	Leg3	12:45:56	23	12.905	53.9	199	295.2	6.9	133.2	213.1	-0.08	36.17	5.47
			-											
			12:55:40											
28	8/29/2018	Leg4	12:57:40	22.86	12.905	53.9	206	295.2	7.3	134.6	33.1	0.03	39.77	5.59
			-											
			13:06:10											
29	8/29/2018	Leg6	13:36:00	21.63	12.915	53.901	2081	283.6	7.9	205.2	32.1	-0.02	49.39	5.47
			-											
			13:42:50											
30	8/29/2018	Leg7	13:44:10	20.46	12.905	53.917	2061	283.6	7.2	208.1	213.1	-0.04	35.18	5.44
			-											
			13:53:00											
31	8/1/2019	Leg1	10:59:30	9.42	12.897	53.208	187	291.8	2.5	318.5	94.0	-0.07	36.11	5.57
			-											
			11:03:30											
32	8/1/2019	Leg2	11:06:25	9.63	12.89	53.206	206	291.8	2.0	311.8	274.1	-0.02	33.47	5.61
			-											
			11:10:55											
33	8/21/2019	Leg1	11:52:00	12.85	12.905	53.202	270	291.2	6.0	275.7	274.6	-0.27	29.55	5.40
			-											
			11:58:30											
34	8/21/2019	Leg2	12:02:00	14.55	12.888	53.206	263	291.2	6.2	272.7	92.9	-0.01	39.95	5.62
			-											
			12:07:30											
35	9/4/2019	Leg1	11:03:00	29.44	12.462	50.143	352	291.2	5.6	213.5	158.7	0.07	28.91	5.92
			-											
			11:16:45											
36	9/4/2019	Leg10	12:58:35	13.96	12.473	50.136	359	292.4	5.5	213	252.0	-0.46	31.17	5.25
			-											
			13:05:00											

	<i>flight date</i>	<i>flight leg</i>	<i>flight time</i>	<i>dist</i>	<i>M(lon)</i>	<i>M(lat)</i>	<i>M(alt)</i>	<i>M(T)</i>	<i>M(wspd)</i>	<i>M(wdir)</i>	<i>M(<math>\chi</math>)</i>	<i>M(w)</i>	<i>M(gs)</i>	<i><math>\alpha_0</math></i>
	<i>d/m/y</i>	-	<i>h:m:s</i>	<i>km</i>	<i>deg</i>	<i>deg</i>	<i>m.a.g.l.</i>	$^{\circ}$ <i>K</i>	<i>m/s</i>	$^{\circ}$	$^{\circ}$	<i>m/s</i>	<i>m/s</i>	-
37	9/4/2019	Leg11	13:06:35	14.53	12.472	50.136	345	292.6	6.3	219.9	72.1	-0.09	37.79	5.77
			-											
			13:12:00											
38	9/4/2019	Leg12	13:13:35	14.51	12.475	50.137	460	292	5.7	209.2	252.2	-0.21	30.84	5.76
			-											
			13:20:10											
39	9/4/2019	Leg13	13:22:30	12.43	12.461	50.16	408	292	6.1	214.3	72.1	-0.06	43.01	5.90
			-											
			13:26:50											
40	9/4/2019	Leg14	13:28:45	12.42	12.461	50.16	358	292.5	5.8	209.1	252.0	-0.51	32.48	5.39
			-											
			13:34:30											
41	9/4/2019	Leg15	13:36:20	13.36	12.462	50.16	412	292.2	6.4	212.1	72.3	-0.36	42.66	5.50
			-											
			13:41:10											
42	9/4/2019	Leg16	13:42:32	13.44	12.462	50.16	301	293.2	5.7	207.7	252.4	-0.52	32.79	5.11
			-											
			13:48:40											
43	9/4/2019	Leg2	11:19:00	29.4	12.457	50.154	407	290.6	6.1	199.1	339.6	-0.33	38.52	5.36
			-											
			11:30:15											
44	9/4/2019	Leg3	11:32:23	29.87	12.461	50.143	391	290.8	5.4	204.8	158.7	-0.32	31.27	5.44
			-											
			11:45:50											
45	9/4/2019	Leg4	11:47:55	29.78	12.456	50.156	391	291	6.3	200.3	338.7	-0.46	36.49	5.23
			-											
			11:59:40											
46	9/4/2019	Leg5	12:02:50	18.13	12.405	50.168	457	291	5.6	205.5	158.8	-0.08	30.59	5.77
			-											
			12:11:10											
47	9/4/2019	Leg6	12:13:20	18.07	12.404	50.169	395	291.4	6.3	202.5	338.4	-0.26	38.21	5.60
			-											
			12:20:30											
48	9/4/2019	Leg7	12:23:00	20	12.404	50.171	345	291.8	5.6	201.1	158.7	-0.31	30.26	5.41
			-											
			12:32:45											
49	9/4/2019	Leg8	12:34:05	19.8	12.406	50.165	443	291.2	6.4	197.4	338.0	-0.05	38.89	5.72
			-											
			12:41:34											
50	9/4/2019	Leg9	12:51:40	13.77	12.47	50.135	461	291.4	6.3	214	72.0	0.1	38.86	6.22
			-											
			12:56:50											
51	9/5/2019	Leg1	09:29:00	28.33	12.464	50.144	566	286	7.2	287.4	158.6	0.13	39	6.01
			-											
			09:40:00											
52	9/5/2019	Leg10	11:26:36	14.41	12.472	50.134	460	287.8	6.8	281.3	252.3	-0.23	27.92	5.60
			-											
			11:34:30											
53	9/5/2019	Leg11	11:36:20	14.09	12.482	50.137	490	287.8	7.4	277.7	72.3	-0.16	42.01	5.92
			-											
			11:41:20											
54	9/5/2019	Leg12	11:43:10	14.11	12.479	50.136	441	288.2	7.3	277.9	252.1	-0.23	30.21	5.69
			-											
			11:50:20											
55	9/5/2019	Leg13	11:52:40	12.91	12.468	50.156	448	288	8.2	273.4	72.2	-0.49	41.28	5.34
			-											
			11:57:30											
56	9/5/2019	Leg14	11:59:05	12.98	12.468	50.156	377	288.6	6.7	275.2	252.4	-0.35	29.26	5.56
			-											
			12:05:40											
57	9/5/2019	Leg15	12:07:35	13.16	12.46	50.153	382	288.6	7.2	278.2	72.1	-0.52	39.85	5.11
			-											
			12:12:40											
58	9/5/2019	Leg16	12:14:15	13.05	12.462	50.154	289	289.4	6.2	279.6	252.0	-0.24	31.42	5.51
			-											
			12:20:40											

	<i>flight date</i>	<i>flight leg</i>	<i>flight time</i>	<i>dist</i>	<i>M(lon)</i>	<i>M(lat)</i>	<i>M(alt)</i>	<i>M(T)</i>	<i>M(wspd)</i>	<i>M(wdir)</i>	<i>M(<math>\chi</math>)</i>	<i>M(w)</i>	<i>M(gs)</i>	<i><math>\alpha_0</math></i>
	<i>d/m/y</i>	-	<i>h:m:s</i>	<i>km</i>	<i>deg</i>	<i>deg</i>	<i>m.a.g.l.</i>	$^{\circ}$ <i>K</i>	<i>m/s</i>	$^{\circ}$	$^{\circ}$	<i>m/s</i>	<i>m/s</i>	-
59	9/5/2019	Leg2	09:42:08	28.66	12.463	50.146	556	286	7.0	277	338.6	-0.11	32.13	5.83
			-											
			09:55:05											
60	9/5/2019	Leg3	09:57:10	29.34	12.465	50.142	533	286.5	6.5	278	158.7	-0.16	36.7	5.80
			-											
			10:09:00											
61	9/5/2019	Leg4	10:11:23	29.48	12.461	50.152	498	287	6.9	274.8	338.5	-0.1	31.55	5.86
			-											
			10:24:55											
62	9/5/2019	Leg5	10:29:00	20.36	12.409	50.164	477	287	7.7	282.4	158.4	-0.22	36.82	5.73
			-											
			10:37:10											
63	9/5/2019	Leg6	10:38:35	20.32	12.408	50.169	489	287	7.1	279.1	338.2	-0.33	27.54	5.57
			-											
			10:48:30											
64	9/5/2019	Leg7	10:49:40	19.48	12.406	50.173	540	286.8	6.7	280.3	158.4	-0.01	37.24	6.19
			-											
			10:57:37											
65	9/5/2019	Leg8	11:00:15	19.51	12.408	50.169	525	286.8	6.2	280.9	338.7	-0.14	27.64	5.92
			-											
			11:09:20											
66	9/5/2019	Leg9	11:18:30	14.2	12.469	50.133	543	287	7.6	280.2	72.1	-0.07	36.02	5.91
			-											
			11:23:50											
67	5/4/2022	Leg1	12:23:15	4.04	12.504	52.11	760	284.6	3.9	148.1	74.7	0.67	36.24	7.01
			-											
			12:25:00											
68	5/4/2022	Leg2	12:26:00	2.86	12.522	52.122	804	283.6	3.8	139.3	265.3	-0.17	39.07	5.32
			-											
			12:27:10											
69	6/14/2022	Leg1	10:05:23	3.02	13.483	53.364	2384	273.2	13.5	315.1	57.5	0.04	30.72	5.57
			-											
			10:06:45											
70	6/14/2022	Leg2	10:07:05	3.12	13.479	53.366	2418	273.2	13.2	321.5	237.3	0.15	39.89	5.71
			-											
			10:08:20											
71	6/15/2022	Leg1	10:11:00	23	12.901	53.892	174	289.5	4.0	277.7	213.2	0.06	32.09	5.72
			-											
			10:21:30											
72	6/15/2022	Leg2	10:24:00	21.58	12.887	53.874	170	289.5	2.6	263.1	33.3	-0.05	31.46	5.42
			-											
			10:33:30											
73	6/15/2022	Leg3	13:48:10	23.13	13.284	53.882	244	290.6	3.5	318.8	197.3	0.07	33.28	5.74
			-											
			13:58:00											
74	6/15/2022	Leg4	14:00:40	22.67	13.281	53.874	247	290.6	2.3	280.2	17.4	0.2	34.87	5.90
			-											
			14:10:30											
75	6/15/2022	Leg5	14:22:15	25.22	12.916	53.884	249	290.6	3.1	337.7	213.0	0.26	34.78	6.05
			-											
			14:32:30											
76	6/15/2022	Leg6	14:35:00	23.33	12.913	53.88	239	290.8	2.3	327.9	33.3	-0.08	26.76	5.39
			-											
			14:46:30											

80 Table S4: General information about the difference in flight conditions between the outbound and return flights (legs).  $\Delta$  values in this table indicate the absolute difference in median conditions between the unbound and the return flight. Symbology: *lon* = longitude, *lat* = latitude; *T* = temperature, *M* = median; *wspd* = windspeed; *alt* = altitude; *wdir* = wind direction,  $\psi$  = heading.

	<i>leg 1</i>	<i>leg 2</i>	<i>flight_date</i>	$\Delta(\text{time})$	$\Delta(\text{alt})$	$\Delta(T)$	$\Delta(\text{wspd})$	$\Delta(\text{wdir})$	$\Delta(\Psi)$
	-	-	<i>m/d/yyyy</i>	<i>s</i>	<i>m.a.g.l.</i>	$^{\circ}K$	<i>m/s</i>	$^{\circ}$	$^{\circ}$
0	Leg1	Leg2	8/14/2017	50	27.56	0.6	0.3	1.1	-0.2
1	Leg3	Leg4	8/14/2017	77	18.79	0.06	0.2	1	0.1
2	Leg5	Leg6	8/14/2017	110	14.67	0.1	0.6	5.5	-3.1
3	Leg7	Leg8	8/14/2017	0	7.46	0.6	0.2	36.2	5.4
4	Leg9	Leg10	8/14/2017	70	171.62	1.3	0.0	7	-0.6
5	Leg1	Leg2	8/15/2017	230	18.27	0.24	1.6	3.8	22.0
6	Leg3	Leg4	8/15/2017	45	48.99	0.6	0.6	7.7	-5.4
7	Leg5	Leg6	8/15/2017	85	3.29	0.3	0.2	5.5	19.5
8	Leg7	Leg8	8/15/2017	175	40.4	0.7	0.7	0.6	4.8
9	Leg9	Leg10	8/15/2017	185	9.84	0.2	1.0	2.7	3.0
10	Leg11	Leg12	8/15/2017	145	13.8	0.1	0.2	1.8	-8.6
11	Leg1	Leg2	8/29/2018	93	27.3	0.4	0.9	0.1	17.6
12	Leg3	Leg4	8/29/2018	74	2.92	0	0.3	1.4	16.1
13	Leg6	Leg7	8/29/2018	120	8.76	0	0.7	2.9	-2.4
14	Leg1	Leg2	8/1/2019	30	12.94	0	0.5	6.7	-2.8
15	Leg1	Leg2	8/21/2019	60	8.97	0.1	0.1	3	2.7
16	Leg1	Leg2	9/4/2019	150	61.25	0.5	0.5	14.4	7.6
17	Leg3	Leg4	9/4/2019	102	18.64	0.2	0.8	4.5	8.1
18	Leg5	Leg6	9/4/2019	70	59.68	0.4	0.7	3	9.9
19	Leg7	Leg8	9/4/2019	136	120.79	0.7	0.9	3.7	9.8
20	Leg9	Leg10	9/4/2019	75	116.71	1	0.8	1	7.2
21	Leg11	Leg12	9/4/2019	70	111.05	0.7	0.6	10.7	6.0
22	Leg13	Leg14	9/4/2019	85	52.29	0.5	0.4	5.2	5.2
23	Leg15	Leg16	9/4/2019	78	122.64	0.9	0.7	4.4	6.8
24	Leg1	Leg2	9/5/2019	117	19.62	0.1	0.3	10.4	17.0
25	Leg3	Leg4	9/5/2019	102	46.7	0.4	0.4	3.2	16.7
26	Leg5	Leg6	9/5/2019	105	19.36	0.1	0.7	3.3	20.0
27	Leg7	Leg8	9/5/2019	68	12.41	0.1	0.5	0.6	16.4
28	Leg9	Leg10	9/5/2019	154	75.39	0.7	0.8	1.1	-13.8
29	Leg11	Leg12	9/5/2019	130	45.45	0.4	0.1	0.2	-11.8



	<i>leg 1</i>	<i>leg 2</i>	<i>flight_date</i>	$\Delta(\text{time})$	$\Delta(\text{alt})$	$\Delta(T)$	$\Delta(\text{wspd})$	$\Delta(\text{wdir})$	$\Delta(\Psi)$
	-	-	<i>m/d/yyyy</i>	<i>s</i>	<i>m.a.g.l.</i>	$^{\circ}K$	<i>m/s</i>	$^{\circ}$	$^{\circ}$
30	Leg13	Leg14	9/5/2019	105	69.86	0.7	1.4	1.8	-12.1
31	Leg15	Leg16	9/5/2019	80	96.55	0.8	1.0	1.4	-10.5
32	Leg1	Leg2	5/4/2022	35	46.8	1	0.1	8.8	-5.7
33	Leg1	Leg2	6/14/2022	7	26.56	0	0.3	6.4	-36.9
34	Leg1	Leg2	6/15/2022	60	1.87	0	1.4	14.6	9.3
35	Leg3	Leg4	6/15/2022	0	1.64	0	1.2	38.6	4.9
36	Leg5	Leg6	6/15/2022	75	17.73	0.2	0.8	9.8	3.5

85

Table S5: General information about the performed pitching maneuvers, including general flight information (date, time height, groundspeed, true airspeed), meteorological conditions (windspeed, wind directions, and wind vector information) and the obtained calibration parameters for  $C_\alpha$ . All wind parameters were calculated after calibration (using average calibration values for 2017/2018 and 2019 - and not with the parameters in the last column). Symbology:  $lon$  = longitude,  $lat$  = latitude;  $T$  = temperature;  $M$  = median;  $wspd$  = windspeed;  $wdir$  = wind direction;  $v_{gs}$  = groundspeed;  $v_{tas}$  = true airspeed;  $\theta$  = Pitch angle;  $C_\alpha$  = calibration value for alpha angle.

95 Table S5 part A

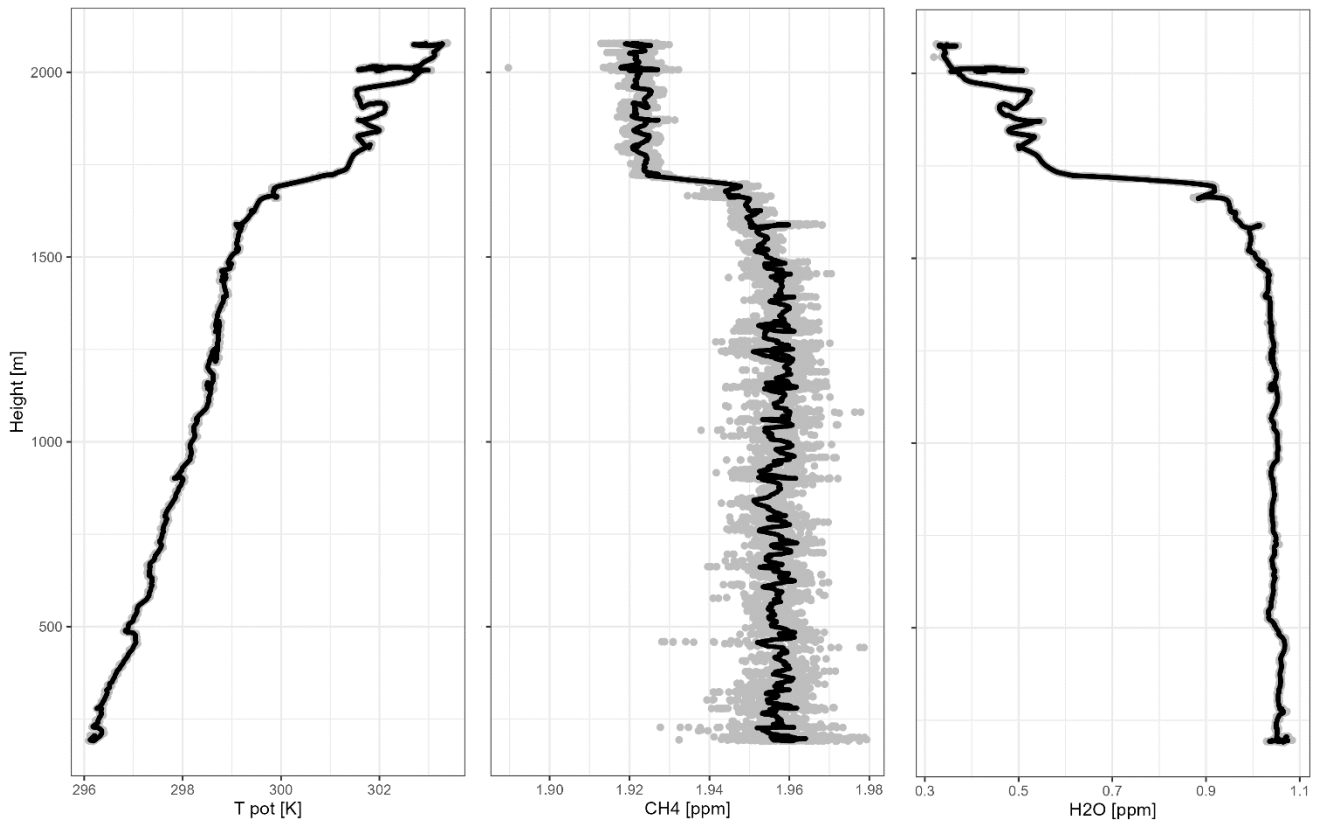
	<i>Flight Date</i>	<i>Flight Time</i>	<i>time</i>	<i>distance</i>	<i>M(lon)</i>	<i>M(lat)</i>	<i>M(height)</i>	<i>M(T)</i>	<i>M(wspd)</i>	<i>M(wdir)</i>
	-	<i>hh:mm:ss</i>	<i>s</i>	<i>km</i>	<i>deg</i>	<i>deg</i>	<i>m.a.s.l.</i>	$^{\circ}\text{K}$	<i>m/s</i>	<i>m/s</i>
1	8/9/2017	17:08:06 - 17:09:08	62	1.73	12.559	52.125	2595.3	279.4	14.39	227.5
2	7/18/2018	10:40:15 - 10:41:37	82	2.36	12.48	52.171	2274.4	280.4	8.8	297.1
3	7/18/2018	10:43:31 - 10:44:33	62	2.74	12.474	52.191	2363.8	279.8	8.66	301.3
4	6/7/2018	18:24:50 - 18:26:17	87	2.58	12.665	52.081	650	295	6.26	114.6
5	9/21/2019	10:15:16 - 10:17:39	143	5.56	12.24	51.948	1036	286.8	0.92	308.4
6	9/21/2019	10:54:32 - 10:55:40	68	2.33	12.543	52.136	1034.9	287	1.49	309.3
7	6/14/2022	10:01:30 - 10:03:20	110	3.07	13.439	53.314	2224.4	274.4	12.24	319.2

Table S5 part B

	<i>Flight Date</i>	<i>M(u)</i>	<i>M(v)</i>	<i>period</i>	<i>M(w)</i>	$\sigma(w)$	<i>M(g<sub>s</sub>)</i>	<i>min(<math>\theta</math>)</i>	<i>max(<math>\theta</math>)</i>	$C_\alpha$
	-	<i>m/s</i>	<i>m/s</i>	-	<i>m/s</i>	<i>m/s</i>		$^{\circ}$	$^{\circ}$	-
1	8/9/2017	10.51	9.7	8.9	1.15	0.25	28.3	-20.1	8.39	0.090
2	7/18/2018	7.93	-4.1	16.4	0.02	0.24	28.2	-27.3	17.08	0.105
3	7/18/2018	7.37	-4.5	12.4	0.38	0.17	43.5	-28	20.3	0.091
4	6/7/2018	-5.73	2.6	14.5	0.11	0.27	29.0	-21.5	12.83	0.093
5	9/21/2019	0.72	-0.6	11.0	0.12	0.15	38.9	-28.6	17.18	0.093
6	9/21/2019	1.13	-0.8	13.6	0.14	0.19	32.9	-30.5	23.57	0.090
7	6/14/2022	7.98	-9.3	18.3	0.25	0.23	27.7	-20.6	15.55	0.131

### **Supplement B: Vertical Flight Profiles**

During several flights, vertical flight profiles were flown to determine the height of the atmospheric boundary layer. Here, we show four vertical profiles flown during two flights over Northeast Germany  
105 (flight dates: 29<sup>th</sup> of August 2018 and 21<sup>st</sup> of August 2019). Abrupt changes in atmospheric chemistry and potential temperature indicate the border of the atmospheric boundary layer.



110 **Figure S1:** First vertical flight profile flown on the 29<sup>th</sup> of August 2018, close to Demmin, Germany  
 (Mecklenburg-Vorpommern). This profile was flown to determine the height of the atmospheric boundary  
 layer, which is defined by abrupt changes in CH<sub>4</sub>, H<sub>2</sub>O and potential Temperature. Grey dots indicate  
 measured variability in concentrations/ temperature at a specific height whereas black lines indicate  
 height averaged concentrations/ temperature. The y-axis represents the measurement height (altitude)  
 115 above ground level.

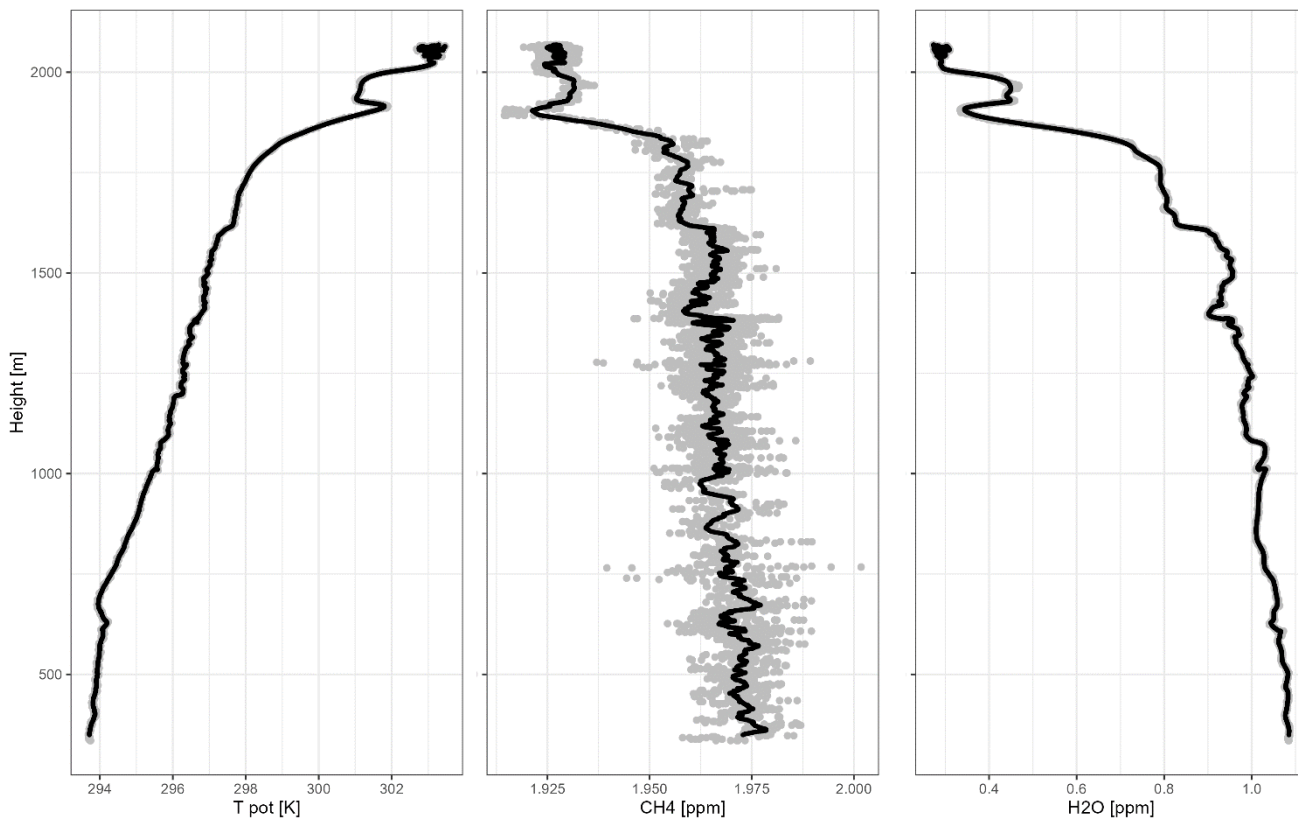
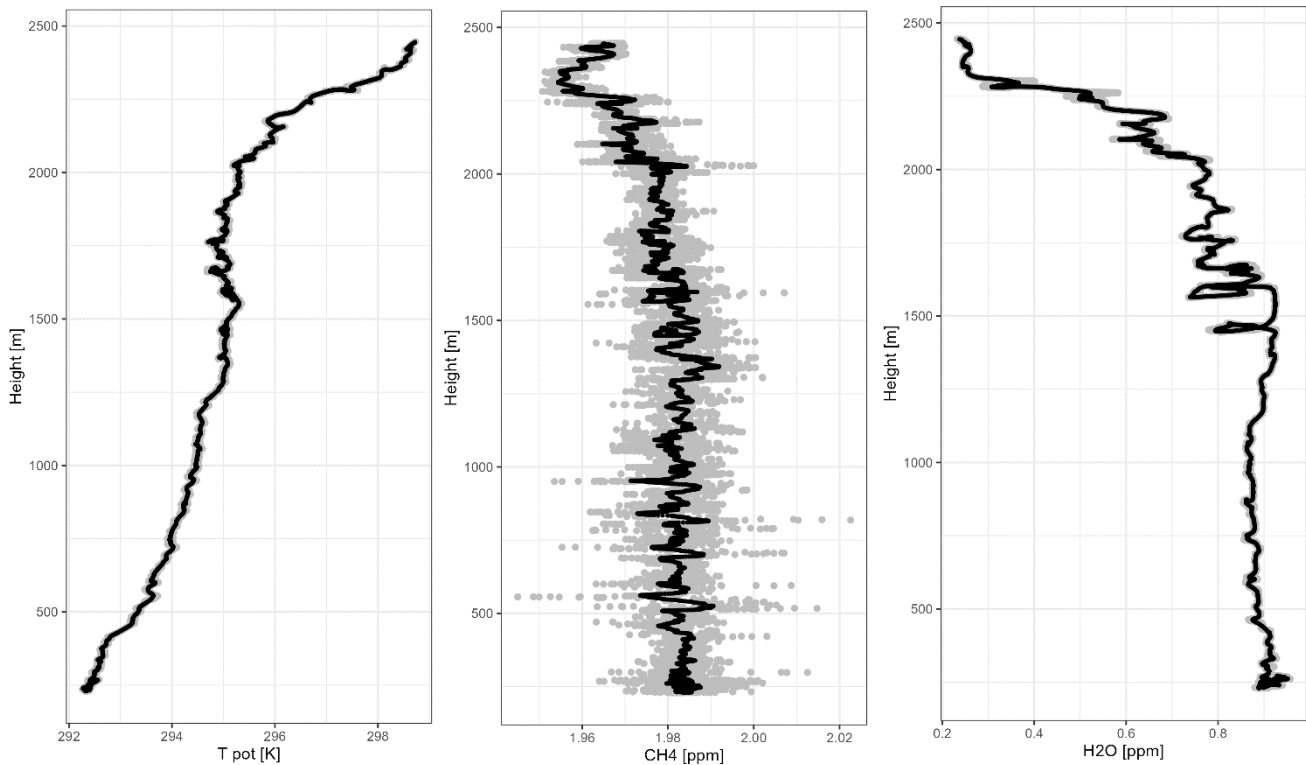


**Figure S2:** Second vertical flight profile flown on the 29<sup>th</sup> of August 2018, close to Demmin, Germany.

120 This profile was flown to determine the height of the atmospheric boundary layer, which is defined by abrupt changes in CH<sub>4</sub>, H<sub>2</sub>O and potential Temperature. Grey dots indicate measured variability in concentrations/ temperature at a specific height whereas black lines indicate height averaged concentrations/ temperature. The y-axis represents the measurement height (altitude) above ground level.

125

130



135 **Figure S3:** First vertical flight profile flown on the 21<sup>st</sup> of August 2019, close to the Müritz national park in Germany. This profile was flown to determine the height of the atmospheric boundary layer, which is defined by abrupt changes in CH<sub>4</sub>, H<sub>2</sub>O and potential Temperature. Grey dots indicate measured variability in concentrations/ temperature at a specific height whereas black lines indicate height averaged concentrations/ temperature. The y-axis represents the measurement height (altitude) above ground level.

140

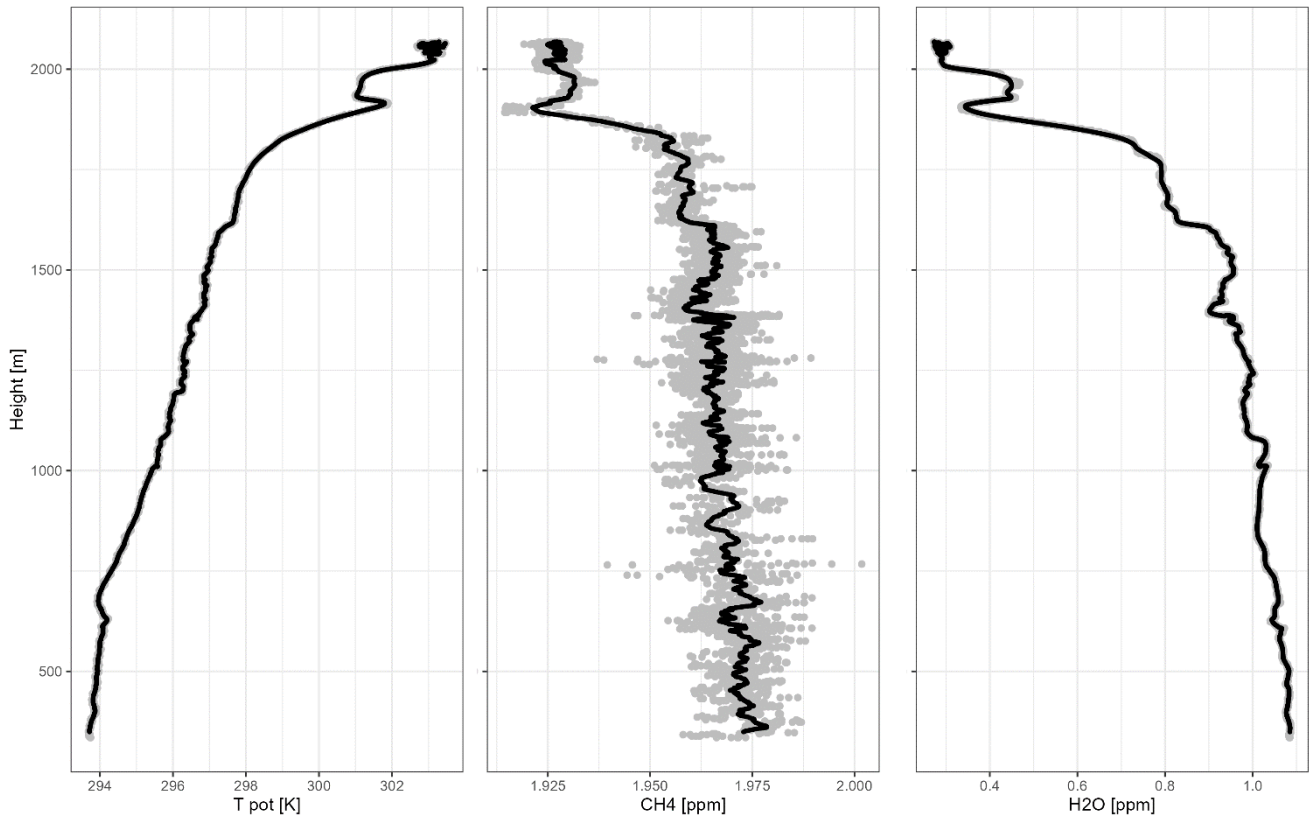


**Figure S4:** Second vertical flight profile flown on the 21<sup>st</sup> of August 2019, close to the Müritz national park in Germany. This profile was flown to determine the height of the atmospheric boundary layer, which is defined by abrupt changes in CH<sub>4</sub>, H<sub>2</sub>O and potential Temperature. Grey dots indicate measured variability in concentrations/ temperature at a specific height whereas black lines indicate height averaged concentrations/ temperature. The y-axis represents the measurement height (altitude) above ground level.